Supplementary Materials for

Colorimetric quantification of linking in thermoreversible nanocrystal gel assemblies

Jiho Kang, Stephanie A. Valenzuela, Emily Y. Lin, Manuel N. Dominguez,
Zachary M. Sherman, Thomas M. Truskett*, Eric V. Anslyn*, Delia J. Milliron*

*Corresponding author. Email: milliron@che.utexas.edu (D.J.M.); anslyn@austin.utexas.edu (E.V.A.);
truskett@che.utexas.edu (T.M.T.)

The PDF file includes:

> Supplementary Text
> Figs. S1 to S31
> Tables S1 and S2
> Legends for movies S1 and S2

Other Supplementary Material for this manuscript includes the following:

> Movies S1 and S2

Table of Contents

1. Synthetic Details

1.1 Tin-doped Indium Oxide (Sn:In$_2$O$_3$, ITO) Nanocrystals

Materials. All chemicals and reagents were used as received without further purification. Indium(III) acetate (99.99%), tin(IV) acetate (> 99.9%), oleic acid (90%, technical grade), and oleyl alcohol (98%) were purchased from Sigma Aldrich. *N,N*-dimethylformamide (DMF, 99%), hexane (99.8%), ethanol (95.0%), and isopropyl alcohol (IPA, 99.5%) were purchased from Fisher Chemical.

Synthesis. ITO nanocrystals were synthesized on a Schlenk line via a simple modification of methods published by the Hutchison group (*34*). First, 0.5 M metal precursor solution was prepared by adding 0.5 mmol tin(IV) acetate, 9.5 mmol indium(III) acetate, and 20 mL oleic acid to a round bottom flask. The precursor solution was heated to 90 °C with stirring and then put under vacuum for 1 hour for degassing. Next, the precursor solution was heated to 150 °C and kept under flowing nitrogen for 3 hours to produce tin(IV) oleate and indium(III) oleate. Meanwhile, 13 mL oleyl alcohol was put into another round bottom flask, heated to 120 °C with stirring, and put under vacuum for 10 min. Then, the oleyl alcohol was heated to 290 °C and kept under flowing nitrogen. 6 mL of the precursor solution was slowly injected into the round bottom flask containing oleyl alcohol using a glass syringe. The injection rate was set to 0.2 mL/min. Once the injection was completed, the reaction mixture was kept at the reaction temperature (290 °C) for 5 min and then cooled down to room temperature. Finally, the nanocrystals were washed 5 times (4 times with ethanol and once with isopropanol) and redispersed in hexane.

Characterization. Size and polydispersity of ITO nanocrystals were determined by small-angle X-ray scattering (SAXS) and scanning transmission electron microscopy (STEM) (*8*).

1.2 Terpyridine-Based Alkyne
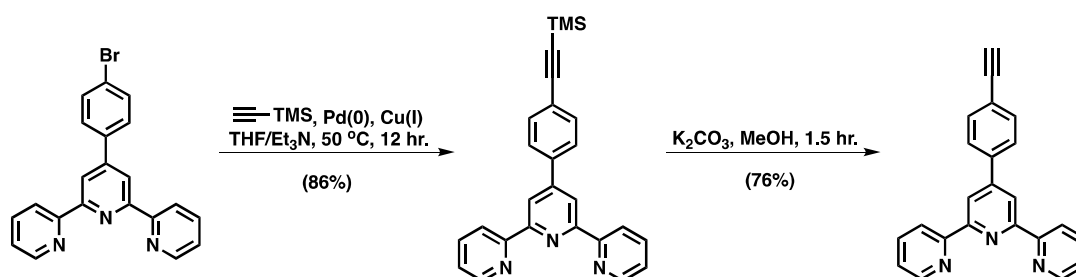
Fig. S1. Synthetic scheme for making the terpyridine-based alkyne. Sonogashira coupling was used to install trimethylsilylacetylene onto the terpyridine-based moiety. This was followed by deprotecting the trimethylsilyl protecting group yielding the terpyridine-based alkyne.

Materials. All materials were used as received unless stated. The (trimethylsilyl)acetylene, 98%, was purchased from Alfa Aesar. 4'-(4-Bromophenyl)-2, 2':6', 2"-terpryidine, >97%, was purchased from Tokyo Chemical Industry Co., LTD. The copper iodide, 99%, and tetrakis(triphenyl-phosphine), 99%, was purchased from Aldrich. Tetrahydrofuran (THF) with 250 ppm BHT, >99%, was purchased from Alfa Aesar. Reagent grade triethylamine (Et$_3$N) and ACS grade solvents (dichloromethane and ethyl acetate) were purchased from Fisher Scientific. Additionally, potassium carbonate was purchased from Fisher Scientific. Sorbtech premium grade silica gel (40-60 mm, 230-400 mesh) was used for flash column chromatography.

Synthesis.

(a) *Sonogashira Coupling Reaction*

A round bottom flask was charged with: 4'-(4-Bromophenyl)-2, 2':6', 2"-terpryidine (0.83 g, 2.45 mmol), copper iodide (16.28 mg, 0.085 mmol), and 100 mL of Et$_3$N/THF (1:1). The solution was degassed with argon for 20 minutes prior to adding tetrakis(triphenyl-phosphine) (0.098 g, 0.085 mmol) and (trimethylsilyl)acetylene (0.70 mL, 5.0 mmol). The reaction was heated to 50 °C for 12 hours. Upon completion, the reaction was diluted in dichloromethane (300 mL) and washed with ammonium chloride (160 mL), followed by a saturated brine solution (80 mL). The organic layer was dried with anhydrous sodium carbonate and concentrated via rotary evaporation. The crude reaction mixture was purified using flash chromatography (99.5:0.5,
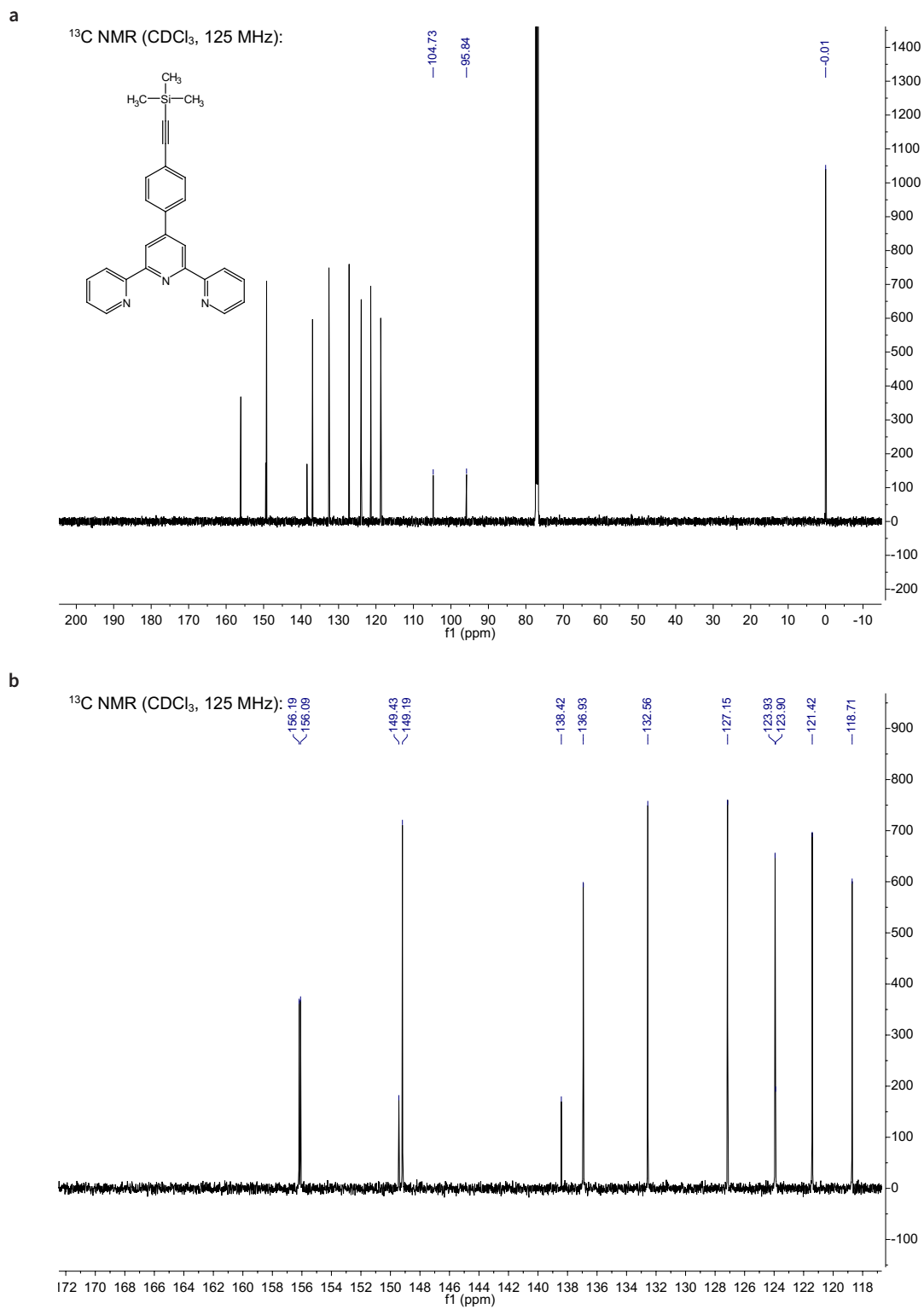
dichloromethane/ethyl acetate) resulting in a tan solid. Yield: 0.86 g (86%). ^{1}H NMR (CDCl$_3$, 500 MHz): δ 8.73 (m, 4H), 8.67 (d, J= 7.9 Hz, 2H), 7.87 (m, 4H), 7.61 (d, J= 8.0 Hz, 2H), 7.36 (m, 2H), 0.28 (s, 9H). ^{13}C NMR (CDCl3, 125 MHz): δ 156.19, 156.09, 149.43, 149.19, 138.42, 136.93, 132.56, 132.56, 127.15, 123.93, 123.90, 121.42, 118.71, 104.73, 95.84, 0.01. HRMS-ESI (m/z): [M]$^+$ cald. for C$_{26}$H$_{23}$N$_3$Si, [M+H]$^+$$_{Theoretical}$= 406.1734, [M+H]$^+$$_{Observed}$= 406.1744, Target Mass Error= -2.37 ppm.

(b) *Trimethylsilyl (TMS) Deprotection*

The TMS-protected terpyridine (0.86 g, 2.1 mmol) was dissolved in 10 mL of dichloromethane and 20 mL of saturated potassium carbonate in MeOH. The reaction was left to stir for 1.5 hrs. Upon completion, the solution was concentrated via rotary evaporation. The product was purified by washing the crude mixture with cold water, and MeOH, resulting in a tan solid. Yield 0.43 g (71%). ^{1}H NMR (DMSO-d$_6$, 500 MHz): δ 8.77 (d, J= 4.2 Hz, 2H), 8.73 (s, 2H), 8.69 (d, J= 7.9 Hz, 2H), 8.05 (t, J= 7.9 Hz, 2H), 7.97 (d, J= 8.4 Hz, 2H), 7.69 (d, J= 8.2 Hz, 2H), 7.54 (m, 2H), 4.37 (s, 1H). ^{13}C NMR (DMSO-d$_6$, 125 MHz): δ 156.31, 155.32, 149.87, 149.00, 138.27, 138.01, 133.18, 127.73, 125.11, 123.29, 121.46, 118.37, 83.49, 82.94. HRMS-ESI (m/z): [M]$^+$ cald. for C$_{23}$H$_{15}$N$_3$, [M+H]$^+$$_{Theoretical}$ = 334.1339, [M+H]$^+$$_{Observed}$ = 334.1346, Target Mass Error = -2.13 ppm.

a

¹H NMR (CDCl₃, 500 MHz):

b
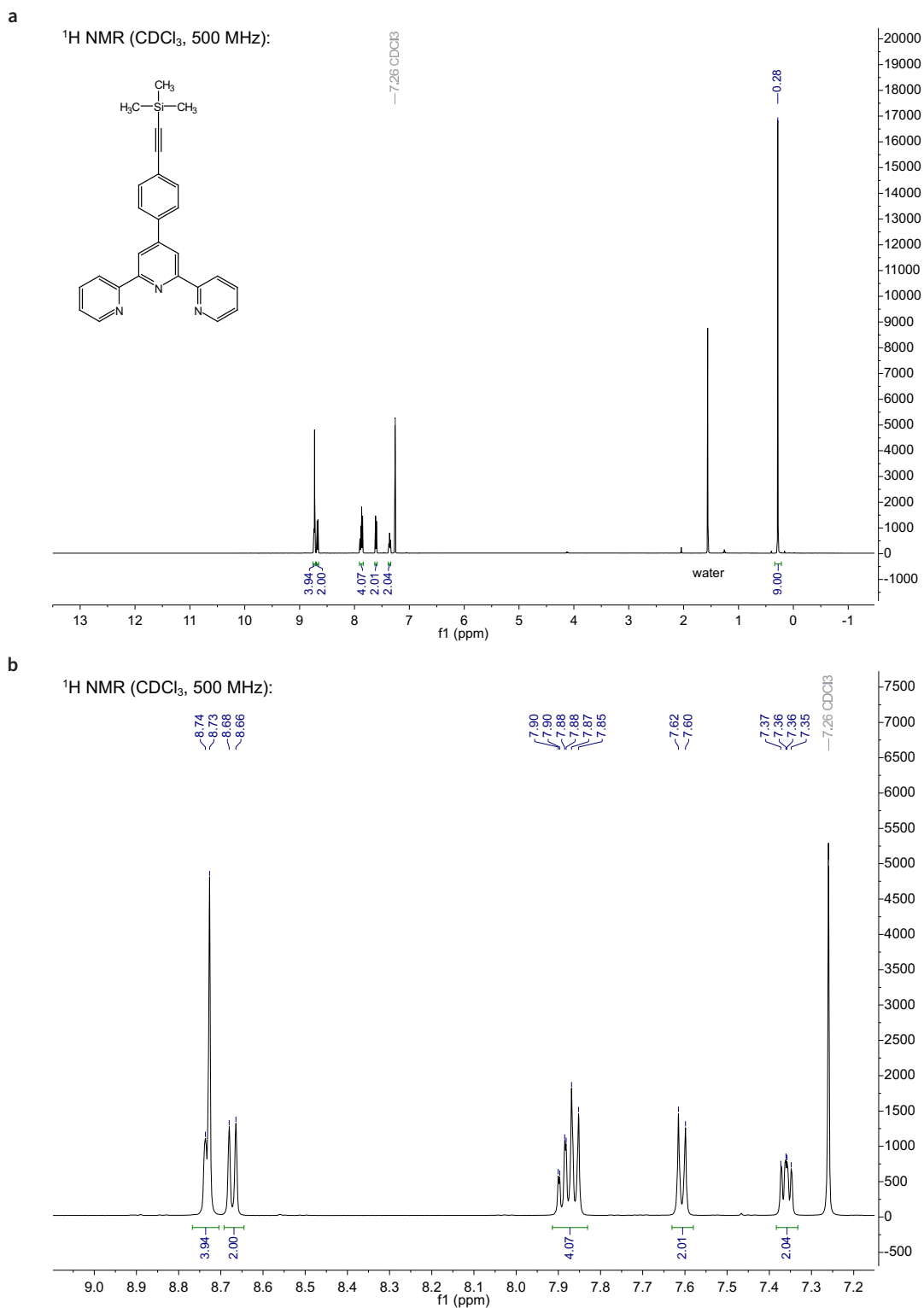
¹H NMR (CDCl₃, 500 MHz):

Fig. S2. ¹H NMR of TMS protected terpyridine-based alkyne (CDCl₃, 500 MHz). (a) Full and (b) magnified spectrum.

a

¹³C NMR (CDCl₃, 125 MHz):

— 104.73
— 95.84
— -0.01

b

¹³C NMR (CDCl₃, 125 MHz):

156.19, 156.09
149.43, 149.19
— 138.42
— 136.93
— 132.56
— 127.15
123.93, 123.90
— 121.42
— 118.71

Fig. S3. ¹³C NMR of TMS protected terpyridine-based alkyne (CDCl₃, 125 MHz). (a) Full and (b) magnified spectrum.

a

¹H NMR (DMSO, 500 MHz):

b

¹H NMR (DMSO, 500 MHz):
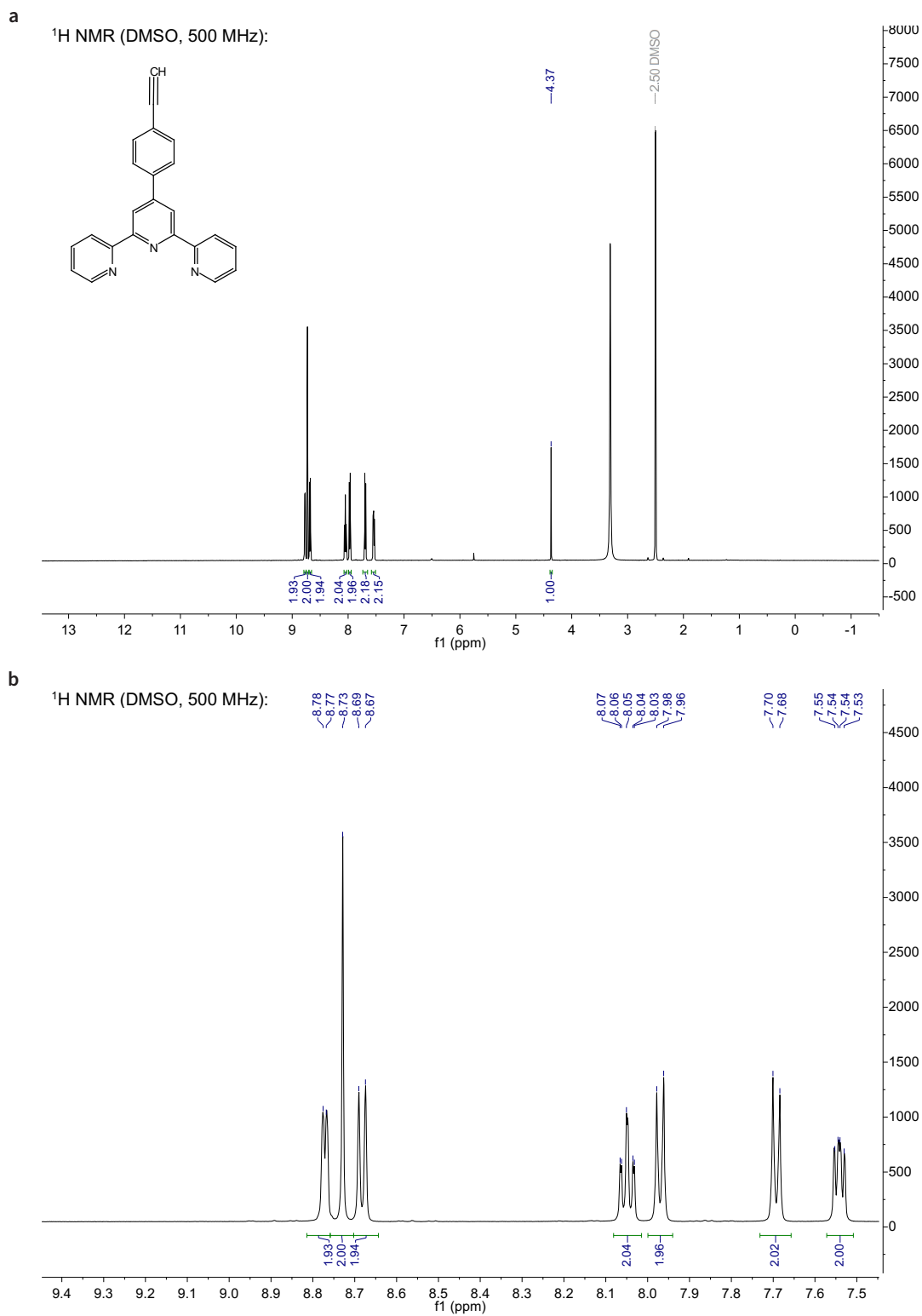
Fig. S4. ¹H NMR of terpyridine-based alkyne (DMSO-d₆, 500 MHz). (a) Full and (b) magnified spectrum.

a

¹³C NMR (DMSO, 125 MHz):

b

¹³C NMR (DMSO, 125 MHz):
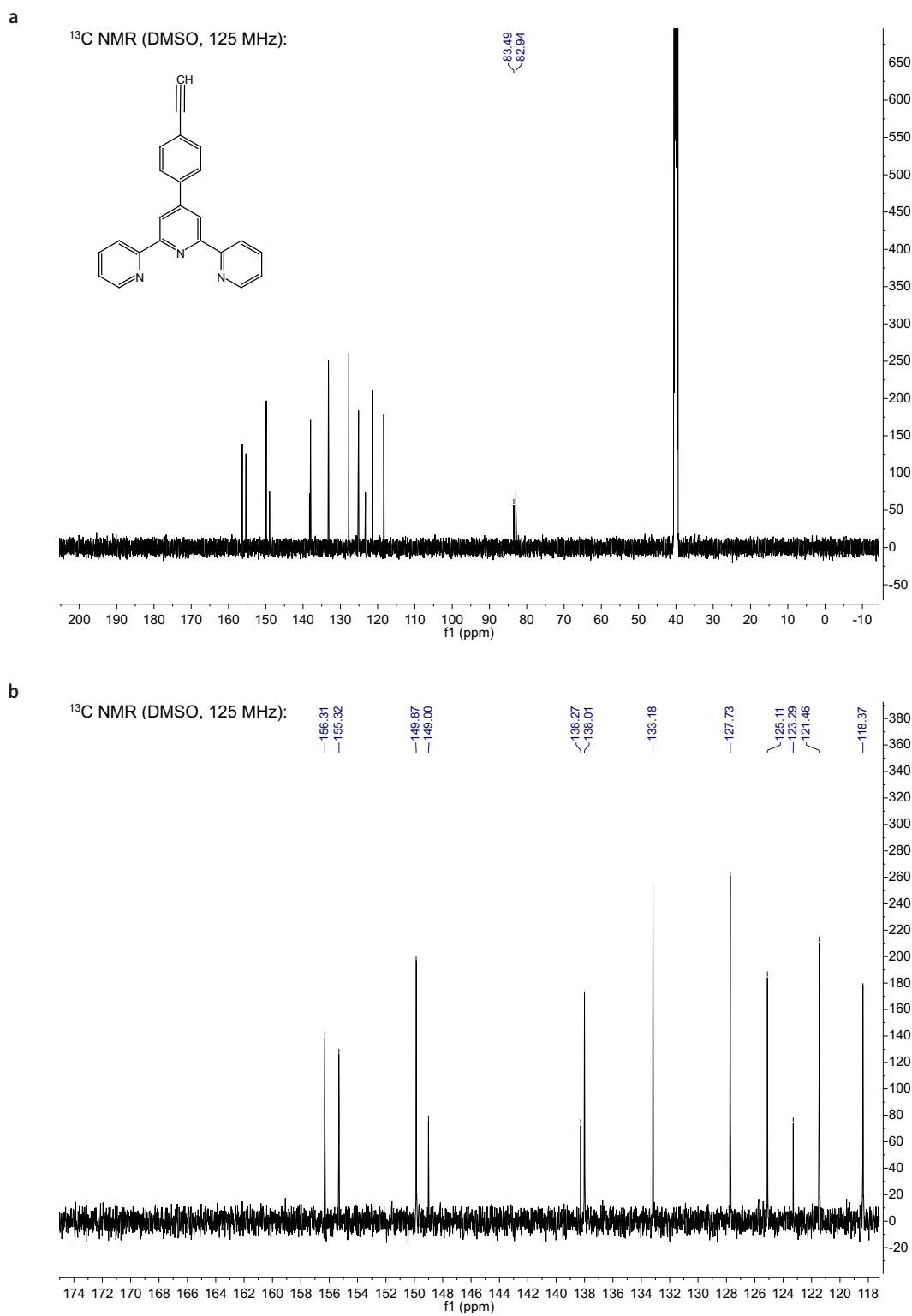
Fig. S5. ¹³**C NMR of terpyridine-based alkyne (DMSO-d₆, 125 MHz).** (a) Full and (b) magnified spectrum.

1.3 Terpyridine-Terminated Ligand (TL)
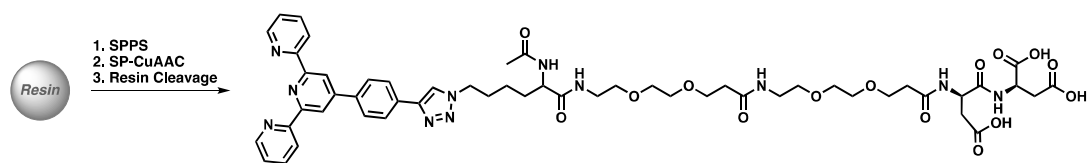
Fig. S6. Synthetic scheme for making the terpyridine ligand (TL). Solid phase peptide synthesis (SPPS) was used to make an azide-terminated ligand. The terpyridine-based alkyne was incorporated onto **TL** using solid phase-copper azide alkyne cycloaddition (SP-CuAAC). The ligand was cleaved from the resin and purified using high performance liquid chromatography (HPLC).

Materials. All materials were used as received unless stated. A baseline correction for all LCMS traces were made using a spline function in Magicplot 3.0. The LCMS traces and mass spectrums were graphed in Igor Pro 8 software to generate the figures.

(a) *Solid phase peptide synthesis (SPPS)*

Fmoc-Asp(O^{t}Bu)- Wang Resin (0.51 mmol/g, mesh 100-200), and Fmoc-Asp(O^{t}Bu)-OH was purchased from P^{3}BioSystems. PurePEG supplied the Fmoc-NH-PEG$_2$-CH$_2$CH$_2$COOH (99.9%). Fmoc-Azido-L-Lysine (99.9%), ethyl(hydroxyamino) cyanoacetate, and *N, N'*-diisopropylcarbodiimide (99.5%) was purchased from Chem-Impex Int'l Inc. ACS grade acetic anhydride, and sequencing grade *N,N*-dimethyl formamide was purchased from Fisher Scientific. Piperidine (99%) was purchased from Alfa Aesar.

(b) *Solid phase copper azide alkyne cycloaddition (SP-CuAAC)*

Copper(I) iodide (99.99%), and (+)-sodium-L-ascorbate (>98%) was purchased from Sigma-Aldrich. Tris(benzyltriazolylmethyl)amine (TBTA) was synthesized using previously published procedures (*8*).

(c) *Resin cleavage cocktail solution*

Trifluoroacetic acid was purchased from Chem-Impex Int'l Inc. Nanopure water was provided by the University of Texas at Austin. Triisopropylsilane (98%) was purchased from

Aldrich Chemistry.

Synthesis. The ligands were readily made exploiting microwave assisted SPPS and SP-CuAAC. The ligands were made using wang resin at a 0.25 mmol scale using a CEM Liberty Blue Automated Microwave Peptide Synthesizer. Standard Fmoc & ^{t}Bu protection strategies were used for the SPPS. Coupling procedures were performed using DIC and Oxyma at 90 °C for 110 seconds. Deprotection of the Fmoc protecting groups were performed using a 20% volume solution of piperidine in DMF in two phases: (1) 75 °C, 155 W for 15 seconds, and (2) 90 °C, 155 W for 50 seconds. Once completed, the resin was subsequentially washed with: DMF, DCM, and MeOH (30 mL each). The resin is then left to dry under vacuum (4-5 hrs).

Once dried, the resin was subject is SP-CuAAC to incorporate the terpyridine moiety. In a 20 mL dram vial, 1.2 equivalents of terpyridine based alkyne, the resulting resin (described in previous paragraph), and 3 mLs of DMF were combined under inert conditions. In a separate round bottom flask, 0.4 equivalents of TBTA, then 0.4 equivalents of sodium ascorbate, and 0.2 equivalents of copper iodide were subsequentially dissolved in 10 mLs of a 4:1 solution of DMF/H_2O under inert conditions. Once dissolved, the solution containing the TBTA, sodium ascorbate, and copper iodide was added to the dram vial containing the resin. The resulting dram vial was put onto an agitator for 12-18 hours under inert conditions. After 12-18 hours, the resin was washed with: DMF, DCM, and MeOH (30 mL each) and dried under vacuum. Once completed, the ligand was cleaved off the resin using 95:2.5:2.5 (TFA/H_2O/TIPS) for 4-5 hours. The residual solution was concentrated, and a white powder was precipitated using ether (35 mL).

The crude mixture was purified using high performance liquid chromatography (HPLC). A Shimadzu Prominence HPLC equipped with a Hichrom C18 preparatory column (Vydac 218TP 10mm, 250 x 22 mm). The HPLC solvents: MeOH and nano-pure water were altered with 0.1% formic acid. The HPLC used a binary gradient of 10% to 95% MeOH over a 90-minute period. The product peaks collected from the HPLC were identified using liquid chromatog-

raphy mass spectrometry (5% to 95% MeOH in a 12-minute gradient, binary solvent system: MeOH/H_2O with 0.1% formic acid). The residual MeOH was removed using rotary evaporation, and the water was removed using lyophilization. This resulted in a light-yellow powder. Yield: 18% (122 mg). HRMS-ESI (m/z): $[M]^+$ cald. for $C_{53}H_{65}N_{11}O_{15}$ $[M+H]^+_{Theoretical} = 1096.4734$, $[M+H]^+_{Observed} = 1096.4749$, Target Mass Error = -1.35 ppm.
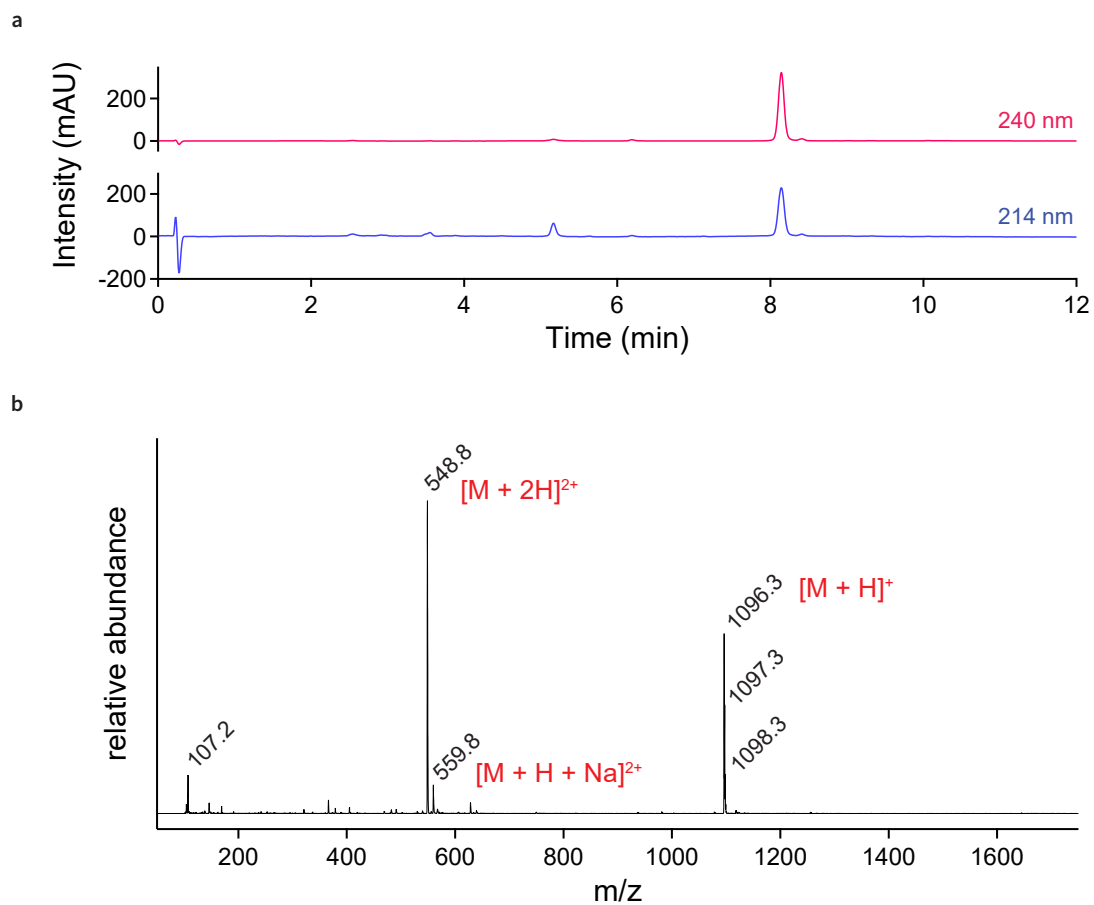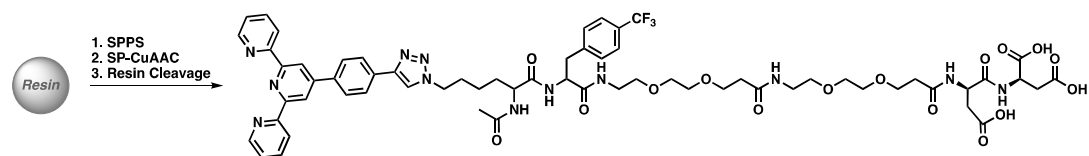
Fig. S7. Characterization of the crude reaction mixture for TL. (a) The LCMS trace and (b) the mass spectrum of the crude reaction mixture for **TL** prior to purification.
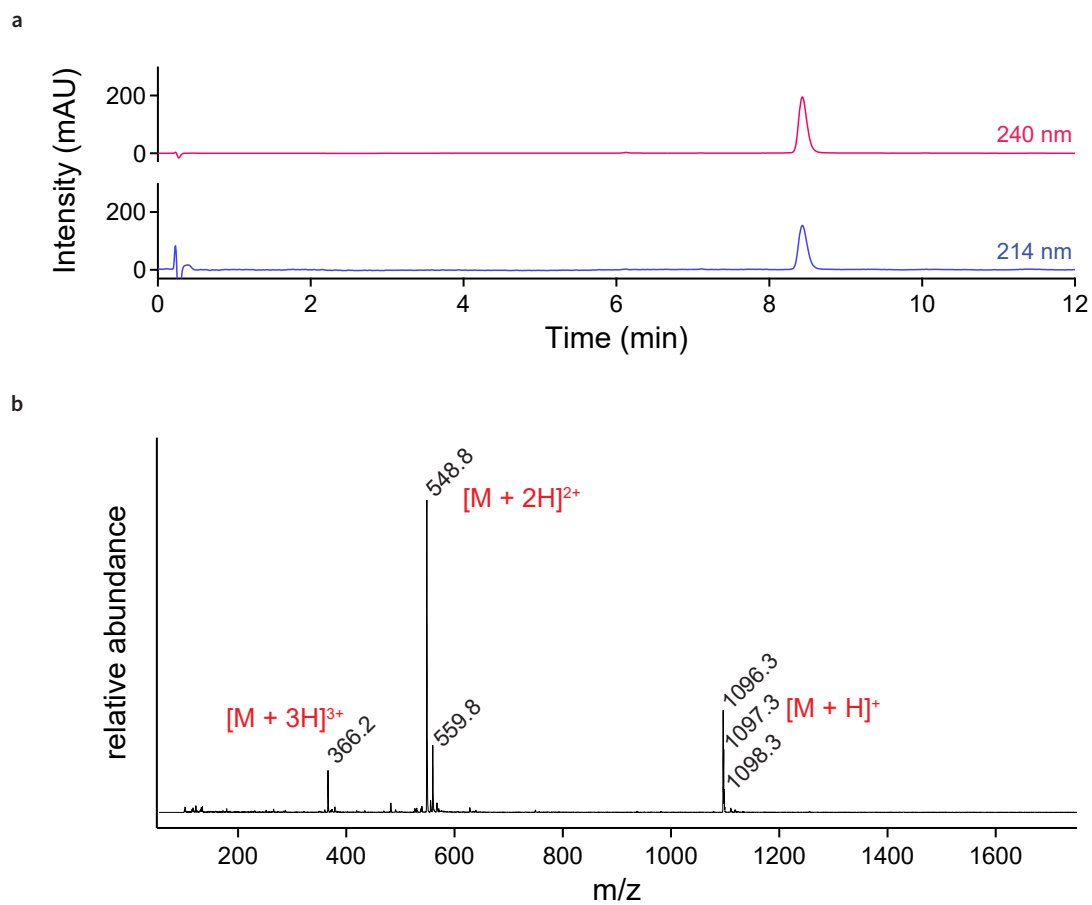
Fig. S8. Characterization of the purified reaction mixture for TL. (a) The LCMS trace and (b) the mass spectrum of the purified reaction mixture for **TL**.

1.4 ^{19}F-Tag Terpyridine Ligand (TL$_{F-Tag}$)


Fig. S9. Synthetic scheme for making TL$_{F-tag}$. Fmoc-4-(trifluoromethyl)-L-phenylalanine was used during the SPPS to create an azide-terminated ligand comprising of a fluorine tag. SP-CuAAC was used to install the terpyridine based moiety onto the terminal end of the fluorinated ligand. The fluorinated ligand was cleaved off the resin and purified using HPLC yielding the desired **TL$_{F-tag}$**.

Materials. The same materials were used as described in synthesizing **TL** except that Fmoc-L-Phe(2-trifluoromethyl)-OH was incorporated for the ^{19}F-label, shown in Figure 9. The Fmoc-L-Phe(2-trifluoromethyl)-OH was used as received and purchased from Chem-Impex Int'l Inc, purity 99.2%. Additionally, a baseline correction for all LCMS traces were made using a spline function in Magicplot 3.0. The LCMS traces and mass spectrums were graphed in Igor Pro 8 software to generate the figures.

Synthesis. The synthesis and purification for **TL$_{F-Tag}$** was identical to the synthesis of TL except for the addition of the ^{19}F-Label described above. The synthesis resulted in a light-yellow powder. Yield: 7.5% (87 mg). HRMS-ESI (m/z): [M]$^+$ cald. for C$_{63}$H$_{73}$F$_3$N$_{12}$O$_{16}$, [M+H]$^+_{Theoretical}$ = 1311.5292, [M+H]$^+_{Observed}$ = 1311.5324, Target Mass Error = -2.38 ppm.

a

b
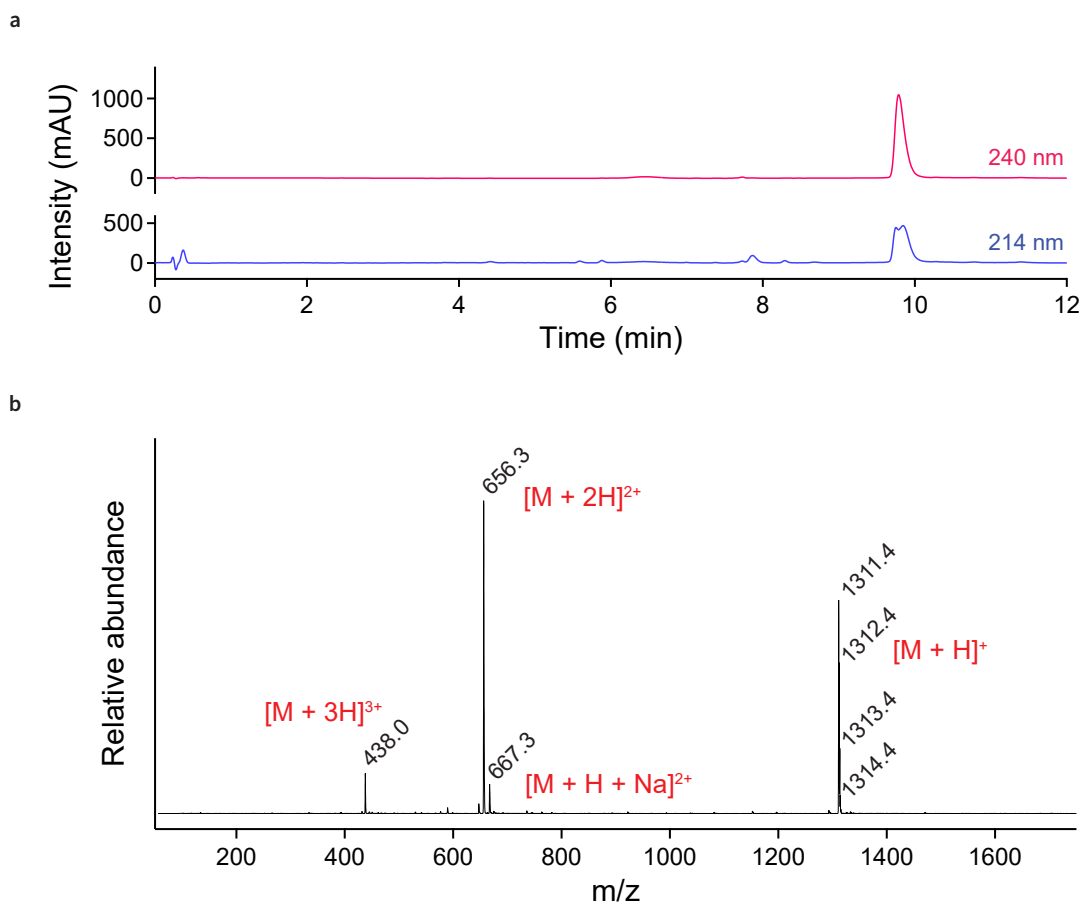
Fig. S10. Characterization of the crude reaction mixture for TL$_{F\text{-tag}}$. (a) The LCMS trace and (b) the mass spectrum of the crude reaction mixture for **TL$_{F\text{-tag}}$** prior to purification.
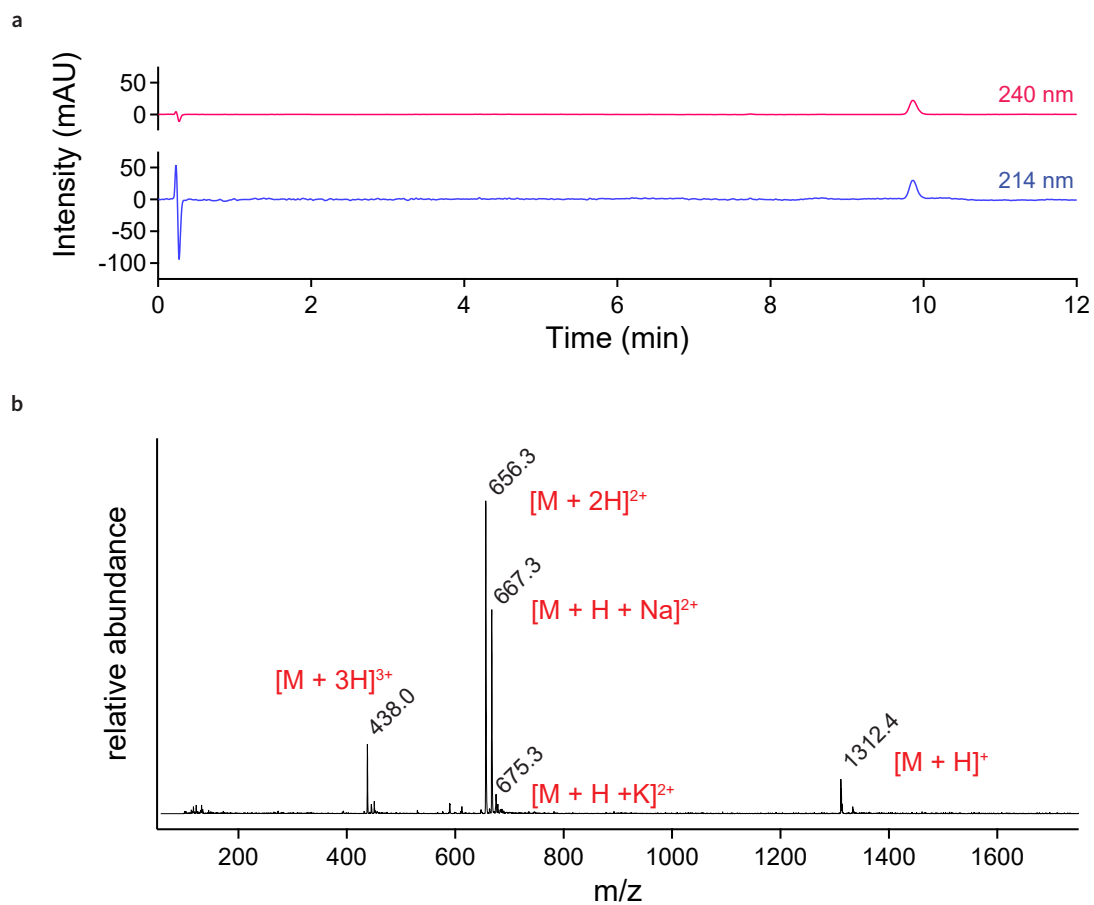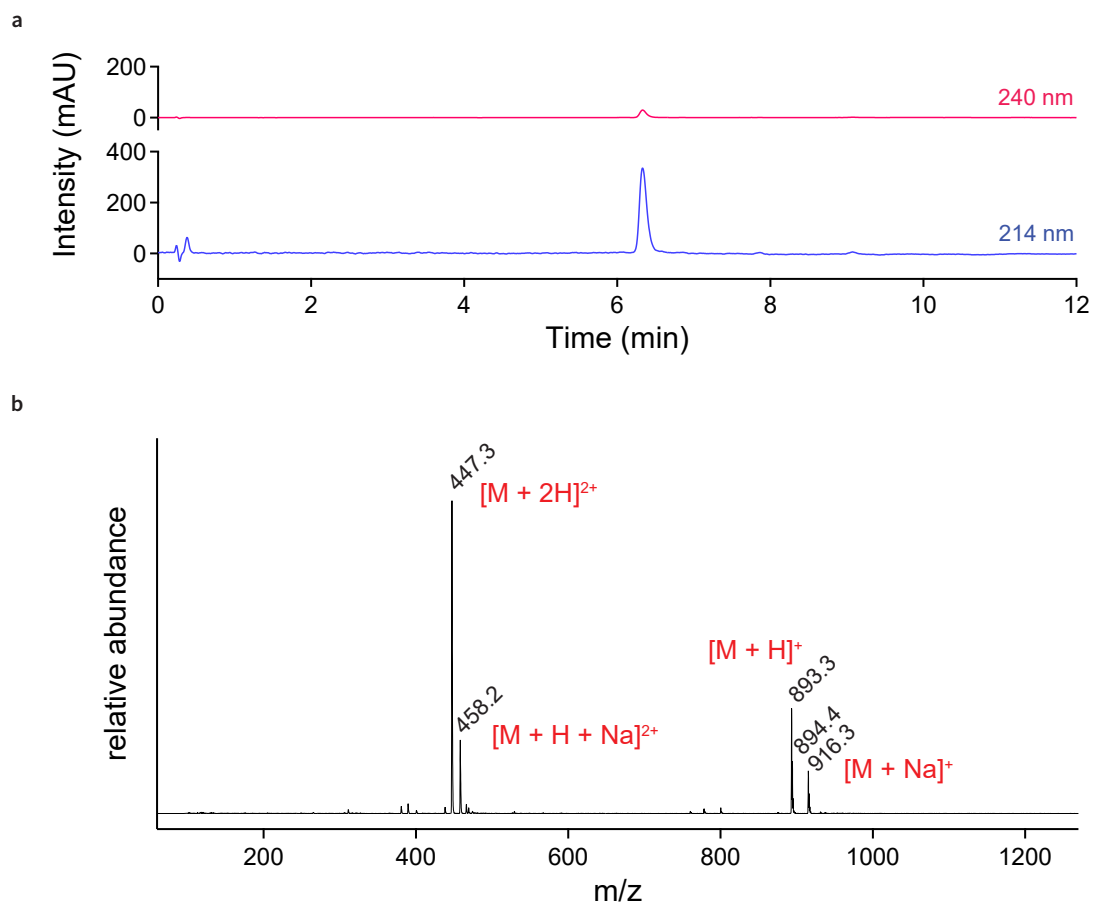
Fig. S11. Characterization of the purified reaction mixture for TL_F-tag. (a) The LCMS trace and (b) the mass spectrum of the purified reaction mixture of **TL_F-tag**.

1.5 Phenyl-Terminated Ligand (PL)

A phenyl-terminated ligand was synthesized using a previously published procedural protocol (fig. S13) (*8*). **PL** was synthesized in a similar manner and scale previously described in Section 1.3. However, 4-phenyl-1-butyne was used during the SP-CuAAC to make **PL**. **PL** resulted in a white powder, with the yield of 23% (50 mg).

Fig. S12. Characterization of the purified reaction mixture for PL. (a) The LCMS trace and (b) the mass spectrum of the purified reaction mixture for **PL**.

2. Instrumentation

2.1 Small-Angle X-ray Scattering (SAXS)

SAXS measurements in transmission mode were performed on the SAXSLAB Ganesha at the University of Texas at Austin, Texas Materials Institute. All samples were contained in flame-sealed glass capillaries (Charles Supper Company, Inc., Boron Rich, 1.5 mm diameter, 0.01 mm wall thickness), including a silver behenate standard used for the calibration of scattering spectra. The sample-to-detector distance was ca. 1 m. SAXS data was processed and analyzed using Igor Pro-based Irena and Nika software. SAXS structure factors were calculated by dividing the measured intensity profile by the form factor derived by fitting the scattering profile of a dilute dispersion of the same nanocrystals (*8*).

2.2 UV-Vis-NIR Spectroscopy

The absorption spectra of oleate-ITO nanocrystals and **TL**-ITO nanocrystals dispersed in hexane and DMF, respectively, were collected on an Agilent-Cary 5000 using a near infrared quartz cuvette (2 mm path length, Spectrocell). *in situ* LSPR absorption spectra of thermoreversible nanocrystal assembly was measured on an Agilent-Cary 5000 using a temperature-controlled liquid cell (Harrick Scientific Products Inc.). All samples were enclosed between two 2-mm-thick CaF_2 windows that were separated by a 56-μm-thick spacer. *in situ* visible absorption spectra of thermoreversible nanocrystal assembly was measured on an Agilent Cary UV-Vis spectrophotometer using a quartz cuvette with 10 mm pathlength. The samples were continuously stirred in a temperature-controlled cuvette holder installed in the spectrophotometer while the spectra were not being collected. In both *in situ* absorption measurements, temperature was kept at each target temperature for 10 min before measurement.

2.3 Fourier Transform Infrared (FTIR) Spectroscopy

FTIR spectra of **TL** and **TL**-ITO were measured at 4 cm^{-1} resolution in transmission configuration with a Bruker Vertex 70 spectrometer. FTIR samples were prepared by drop-casting

dilute solutions of **TL** or **TL**-ITO in DMF (0.2 mg/mL) onto double side polished silicon wafers and drying them in ambient air.

2.4 Scanning Transmission Electron Microscopy (STEM)

STEM imaging was carried out using a Hitachi S5500 scanning transmission electron microscope (STEM). All images were obtained in the STEM mode at an accelerating voltage of 30 kV. A dispersion of oleate-ITO dispersed in hexane was drop casted onto carbon-coated 400 mesh copper grids. A dispersion of **TL**-ITO in DMF and a solution of nanocrystal gel in DMF were drop casted onto silicon nitride support films (3 X 3 array of 0.1 X 0.1 mm window).

2.5 Nuclear Magnetic Resonance (NMR) Spectroscopy

^{1}H NMR of **TL**-ITO and ^{19}F NMR of **TL$_{F\text{-}Tag}$** and **TL$_{F\text{-}Tag}$**-ITO were measured on a MR 400 NMR spectrometer at 400 MHz using a OneNMR probe with Protune accessory. NMR spectra were acquired with a relaxation delay of 2 s (1 s for ^{19}F), an acquisition time of 4 s (1 s for ^{19}F), a total of 64 scans (128 for ^{19}F), and a pulse angle of 30 ° (90 ° for ^{19}F), and their chemical shifts were calibrated to respective solvent peaks.

^{1}H and ^{13}C NMR of all ligands and their synthetic intermediates were acquired using Prodigy Cryoprobe Bruker Avance III 500 with a relaxation delay of 1 s (2 s for ^{13}C) and a total of 32 scans (1024 scans for ^{13}C). All NMR data was processed by MestreNova.

3. Experimental Methods

3.1 Ligand Functionalization Procedure

ITO nanocrystals in hexane were flocculated using isopropanol, centrifuged, and dried into a nanocrystal pellet. A solution of **TL** or **TL$_{\text{F-Tag}}$** (0.01 M) in DMF was added to the dried pellet and the solution was sonicated for 1 hour (nanocrystals were well-dispersed within 5 min of sonication). The solution was left overnight, washed 3 times using a 3:7 mixture of isopropanol:hexane, and dispersed in neat DMF.

3.2 Quantification of Bound Ligands

The average number of bound ligands per nanocrystal was quantified using **TL$_{\text{F-Tag}}$** and ^{19}F NMR, following a previously established protocol (*8*). The concentration of bound **TL$_{\text{F-Tag}}$** was calculated by comparing its integral of the peak (-59.1 ppm) with that of a known concentration of trichlorofluoromethane (CFCl$_3$, 10 mM, -1.10 ppm). The concentration of nanocrystals was determined by weight.

3.3 Preparation of Samples for Optical Monitoring

Nanocrystal assembly was induced at room temperature by adding tetrabutylammonium chloride (TBACl, 0.5 M, in DMF) and cobalt(II) chloride (CoCl$_2$, anhyd., 0.01 M, in DMF) to a stock solution of **TL**-ITO (43.0 mg/mL, 0.6 vol%, in DMF). The final volume fraction of nanocrystals was adjusted to 0.1 % by adding neat DMF. The concentration of CoCl$_2$ was fixed at 0.5 mM, while that of TBACl was varied between samples ([TBACl] = 100, 150, and 200 mM). Control samples were prepared in the same conditions except that nanocrystals functionalized with a phenyl-terminated ligand (**PL**), which otherwise has the same structure as **TL**, were used instead of **TL**-ITO.

3.4 Deconvolution of *in situ* Visible Absorption Spectra

The amount of bound and free Co^{2+} in free-flowing nanocrystal dispersions was quanti-

fied via deconvolution of *in situ* visible absorption spectra (fig. S26). The visible absorption of free-flowing nanocrystal dispersions can be attributed mainly to ITO nanocrystals (bandgap and LSPR), bound Co^{2+}, and free Co^{2+}. First, the contribution from ITO nanocrystals was removed by subtracting the absorption spectra of **TL**-ITO dispersions from those of free-flowing nanocrystal dispersions, leaving absorption due to bound and free Co^{2+} (step **i**). Next, the spectra between 750 to 800 nm were fitted with a linear baseline, which was then extrapolated down to 693 nm (step **ii**). The peak intensity of deconvoluted free Co^{2+} (I_s) was determined by subtracting the value of the extrapolated linear fit at 693 nm from that of the total absorption spectra of bound and free Co^{2+}. Next, visible absorption spectra of control samples were obtained and their absorption intensity at 693 nm (I_o) was found (step **iii**). Deconvoluted absorption spectra of free Co^{2+} were obtained by scaling down the absorption spectra of the solutions containing only free Co^{2+} with the factor of I_s/I_o (step **iv**). Lastly, deconvoluted absorption spectra of bound Co^{2+} were obtained by subtracting the deconvoluted spectra of free Co^{2+} from the total absorption spectra of bound and free Co^{2+} (step **v**).

3.5 Molecular Dynamics Simulations Molecular dynamics simulations were performed using a coarse-grained model recently shown to qualitatively reproduce theoretically predicted and experimentally observed behaviors of linker-mediated gels of colloidal nanocrystals (*8*). Nanocrystals, ligands, and linkers in the model were represented explicitly with physical dimensions approximating those of the experimental system, while the solvent was treated implicitly (fig. S28).

We considered a linker-to-nanocrystal ratio of $\Gamma = 250$, and grafted 600 ligands to each nanocrystal surface. The nanocrystal was modeled as a smooth, spherical particle of diameter $d_p = 17.4\sigma$ and mass $m_{NC} = 5294m$. Ligands were modeled as linear bead-spring chains with seven beads, each has a diameter of $d_m = \sigma$. One terminal bead of each ligand was fixed to its location on a nanocrystal surface by a rigid bond. The terminal bead on the ligand's opposite free end was bonded to a type A "patch" that could interact favorably with a type B patch on

a linker to mimic the dynamic coordination reaction. Type B patches were similarly bonded to opposite ends of a linker bead. Type A and B patches have a diameter of $d_p = 2/3\sigma$. The ligand bead, the linker central bead, and the patches each have a mass of m. (Figure S28)

All intramolecular bonds used in our model are described by a harmonic potential

$$u_b(r_{ij}) = \frac{k_b}{2} (r_{ij} - b_o)^2 \tag{1}$$

with spring constant $k_b = 600 k_B T / \sigma^2$. The equilibrium bond length for ligand-ligand bonds was set to $b_o = 0.96\sigma$, and that for the ligand-patch bonds was set to $b_o = 2^{1/6}/2$. Additionally, the angles between the type A "patch" and the ligand's penultimate bead, and the angle between the two type B "patches" on a linker molecule were restrained to 180° using a harmonic bending potential

$$u_\theta(\theta) = \frac{k_\theta}{2} (\theta - \pi)^2 \tag{2}$$

where $k_\theta = 600 k_B T$ is the spring constant, k_B is the Boltzmann constant and T is temperature.

The non-bonded interaction between the two types of patches was simulated using the cut and shifted Lennard-Jones (LJ) interaction potential

$$u_{ij}(r_{ij}) = -4\epsilon \left[\left(\frac{\sigma_{ij}}{r_{ij}}\right)^{12} - \left(\frac{\sigma_{ij}}{r_{ij}}\right)^6 \right] - u_{cut}(r_{cut}) \tag{3}$$

where ϵ and σ_{ij} set the energy and length scales for the interactions, and r_{cut} is the cutoff length. For the attractive interaction between patches A and B, we varied the magnitude of ϵ_b to simulate different system temperatures. We also set $\sigma_{AB} = 0.2\sigma$, and $r_{cut,AB} = 1.0\sigma$. The repulsive interaction between patches of the same type has $\epsilon_{AA} = \epsilon_{BB} = 1.0 k_B T$, $\sigma_{AA} = \sigma_{BB} = 2/3\sigma$, and $r_{cut,AA} = r_{cut,BB} = 2^{1/6}\sigma_{AA}$. We used larger σ_{AA} and σ_{BB} relative to σ_{AB} to prevent multiple B patches coordinating to the same A patch.

All other non-bonded interactions were purely repulsive and simulated using the core-shifted LJ potential

$$u_{nb}(r_{ij}) = -4\epsilon \left[\left(\frac{\sigma_{ij}}{r_{ij} - \delta_{ij}}\right)^{12} - \left(\frac{\sigma_{ij}}{r_{ij} - \delta_{ij}}\right)^6 \right] - u_{cut}(r_{cut}) \tag{4}$$

with $\epsilon = 1.0 k_B T$, and $\delta_{ij} = (\sigma_i + \sigma_j)/2 - \sigma$ shifts the location of the potential divergence to account for the different diameters of the particles. The cutoff distances are set at the minimum of the potential, $r_{cut} = 2^{1/6} + \delta_{ij}$, thereby eliminating the attractive part of the potential.

Molecular dynamics simulations were performed with LAMMPS (9 January 2020) (*47*) using an integration time step of 0.0025τ, where $\tau = \sqrt{m\sigma^2/\epsilon_b}$, coupled with a Nose-Hoover thermostat with a time constant of 0.25τ at constant volume. Nanocrystal-linker mixture simulations considered 100 nanocrystals in a cubic simulation cell with an edge length of $L \approx 240\sigma$ ($\eta_{NC} = 0.02$) and triply periodic boundary conditions to mimic bulk systems. First, equilibration was performed for $6.25 \times 10^5 \tau$ with purely repulsive non-bonded interactions between all particles and patches. After equilibration, attraction between patches of type A and B were turned on, and different $k_B T/\epsilon_b$ were investigated to explore the effects of temperature. For each case, the nanocrystal-linker mixture was simulated for an additional $6.25 \times 10^5 \tau$ to collect information on the location of each particle and patch. We defined the fraction of bound linkers as

$$f_l = 1 - N_{\text{l, free}}/N_{\text{l, total}} \tag{5}$$

where $N_{\text{l, free}}$ is the number of linkers that are not attached to any ligands, and $N_{\text{l, total}}$ is the total number of linkers in the simulation.

We quantified the different bonding motifs throughout the simulations. A single bond is defined as a linker-ligand bond with the other linker patch being free. If k links are formed between two nanocrystals, then $k - 1$ links are treated as redundant bonds, and one link is counted as an effective bond. Uniquely bound linker between ligands from two nanocrystals are also defined as an effective bond. Given $N_{\text{l, total}}$ bound linkers, we define the fraction of each bonding motif (x) as

$$f_x = N_x/(f_l \cdot N_{\text{l, total}}) \tag{6}$$

where N_x is the number of linkers in bonding type of x.

Lastly, nanocrystals were considered part of a given cluster if they were connected to another nanocrystal in that cluster by at least one linker.
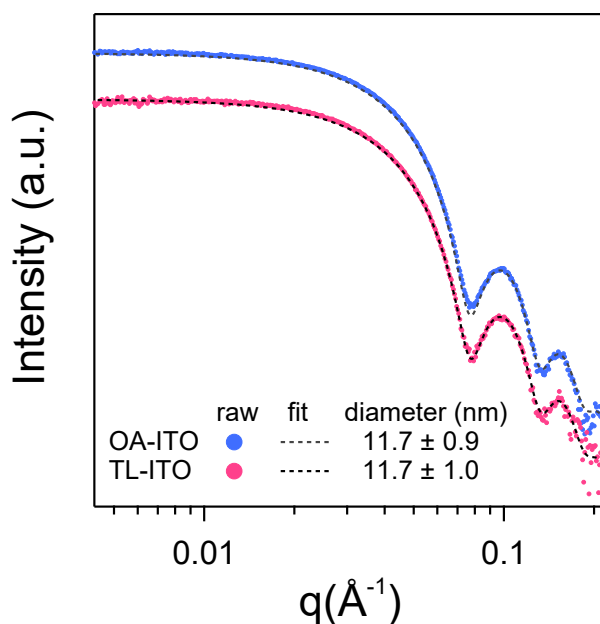
4. Supplementary Figures and Tables
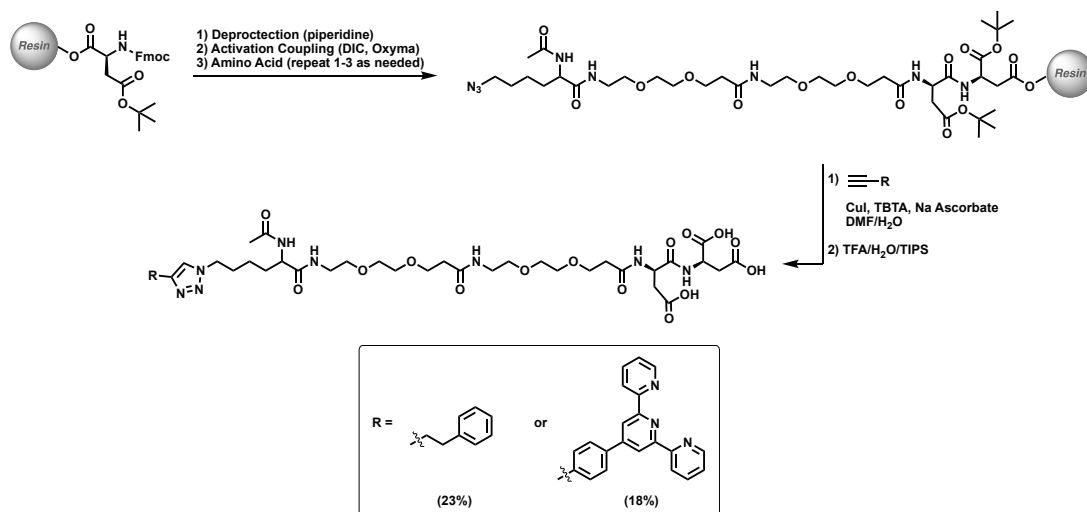
Fig. S13. Overall synthetic scheme to make TL and PL. Terpyridine-based alkyne and 4-phenyl-1-butyne were used duing SP-CuAAC for synthesis of **TL** and **PL**, respectively.
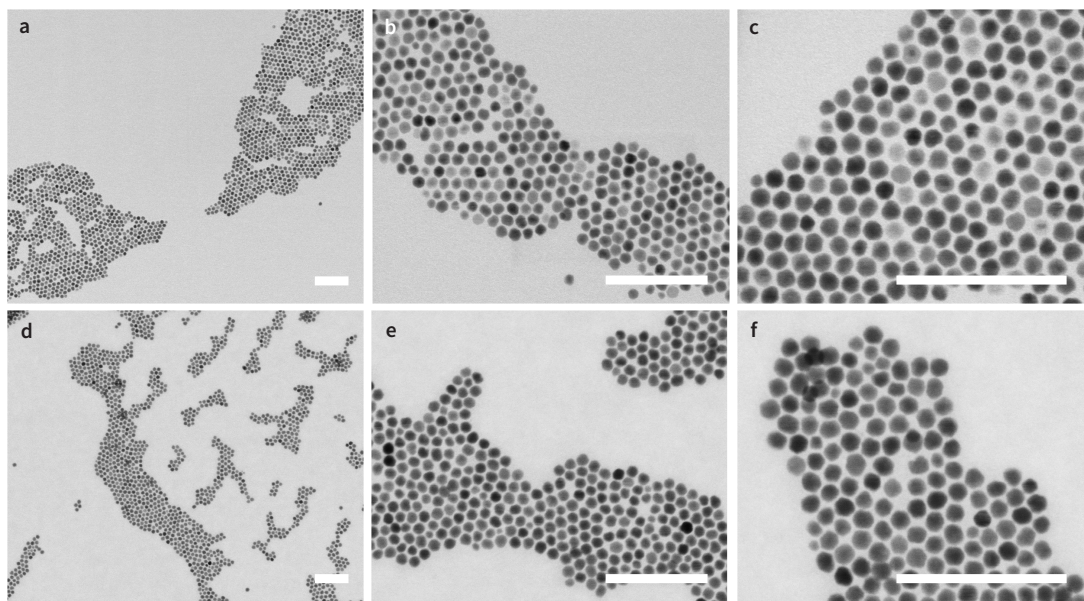

Fig. S14. STEM images of ITO nanocrystals before and after TL-functionalization. (a-c) Oleate capped-ITO and (d-f) **TL**-ITO. Scale bars are 100 nm.

Fig. S15. Size analysis of ITO nanocrystals by SAXS before and after TL-functionalization. The scattering curves of nanocrystal dispersions were fit with a spheroid form factor with a Gaussian distribution of sizes.
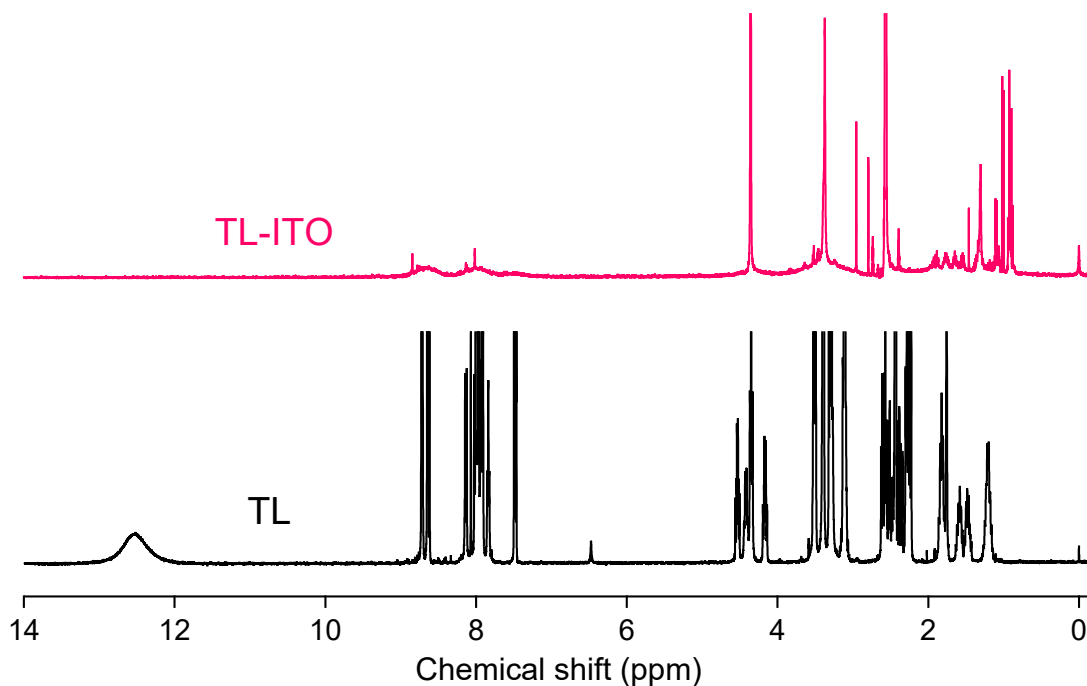
Fig. S16. Full ^{1}H NMR spectra of TL and TL-ITO. Note that a broad peak at 12.5 ppm assigned to the carboxylic hydrogens of **TL** is absent and multiple peaks from 7.4 to 8.8 ppm characteristic of terpyridine are significantly broadened and shifted in **TL**-ITO.
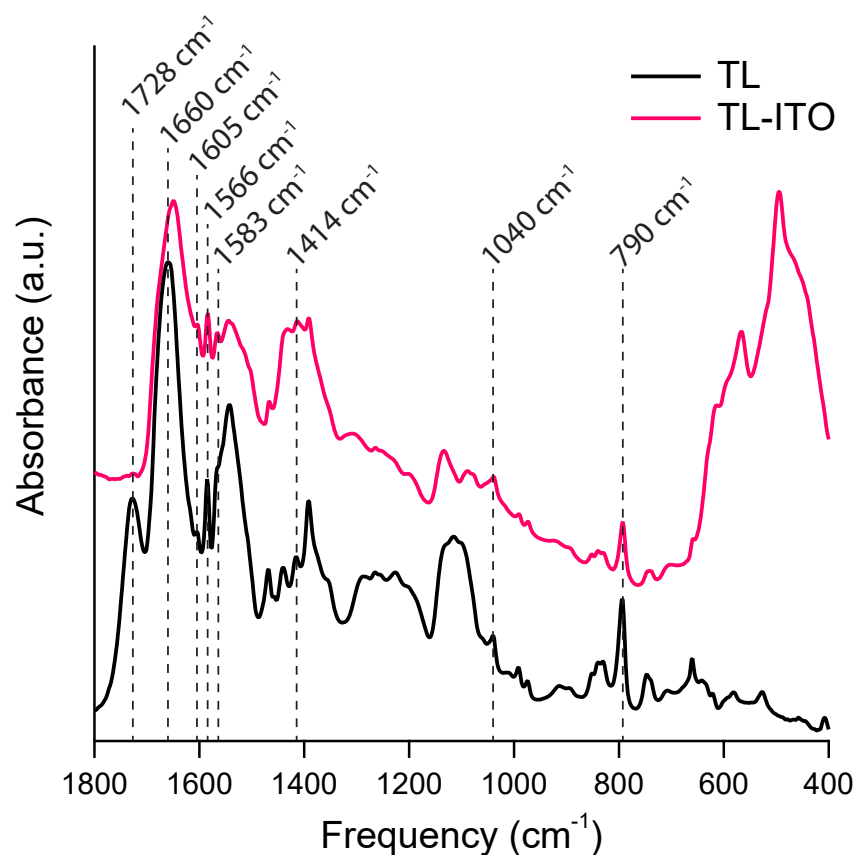
Fig. S17. FTIR spectra of TL and TL-ITO. 1728 cm^{-1}, v(C=O) of carboxylic acid; 1650~1660 cm^{-1}, carbonyl and amide group; 1605 cm^{-1}, v(C=C) of aromatic ring; 1583 cm^{-1}, δ(N-H) of amide(II); 1566 cm^{-1}, v(C=N) of pyridine; 1414 cm^{-1}, v_s(C-O) of PEG; 1040 cm^{-1}, v_{as}(C-O) of PEG; 790 cm^{-1}, v(C-C) between pyridine rings. Peaks consistent with v(C=O) of bound carboxylate are present in the spectrum of **TL**-ITO, but they overlap with other fingerprint peaks and cannot be uniquely assigned.
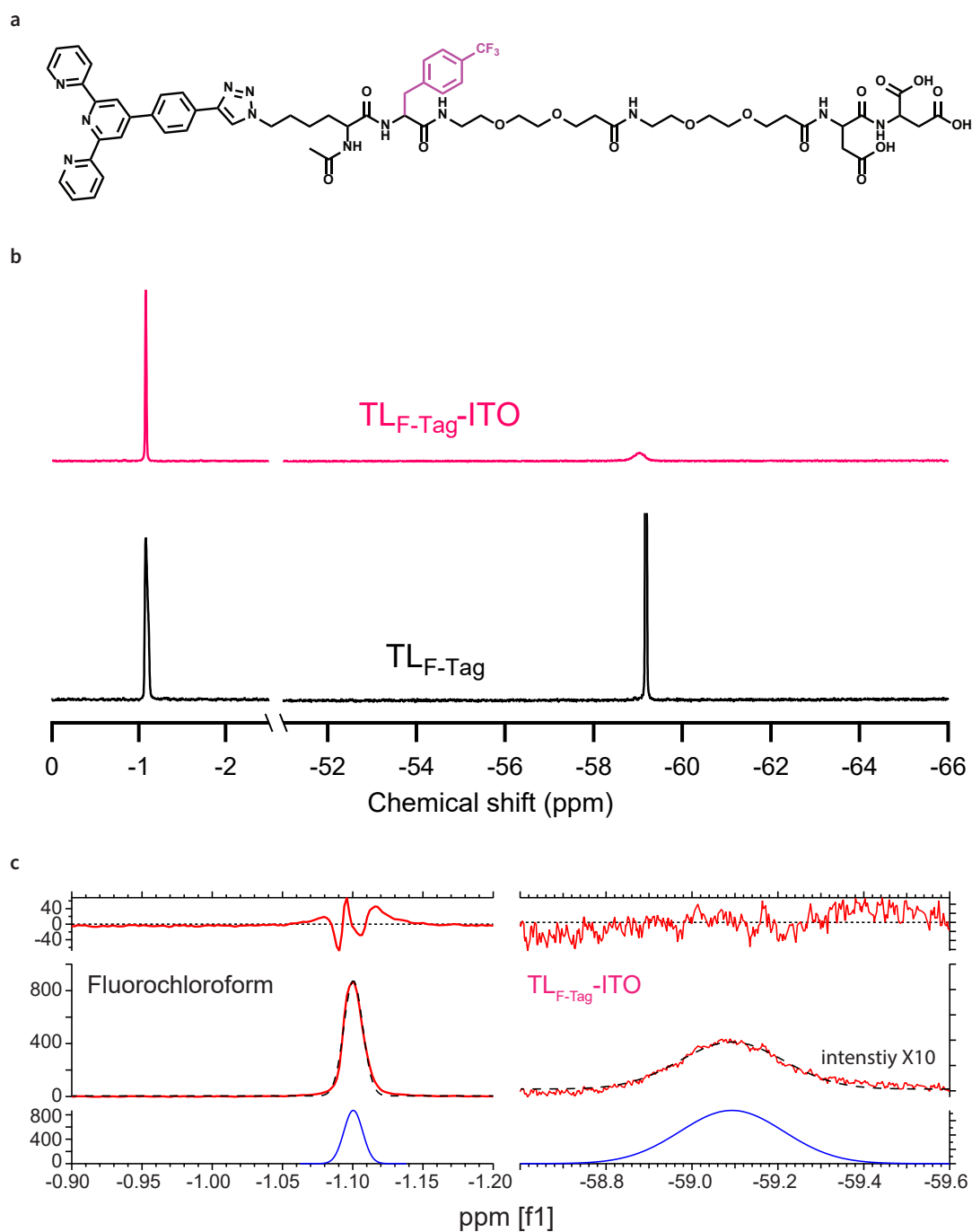
**Fig. S18. ¹⁹F NMR to quantify the number density of TL on nanocrystals.** (a) Molecular structure of fluorine tagged-**TL** (**TL$_{F\text{-Tag}}$**). (b) ¹⁹F NMR spectra of **TL$_{F\text{-Tag}}$** and ITO nanocrystals functionalized with **TL$_{F\text{-Tag}}$**. (c) Gaussian fitting of ¹⁹F NMR spectra for ligand quantification.
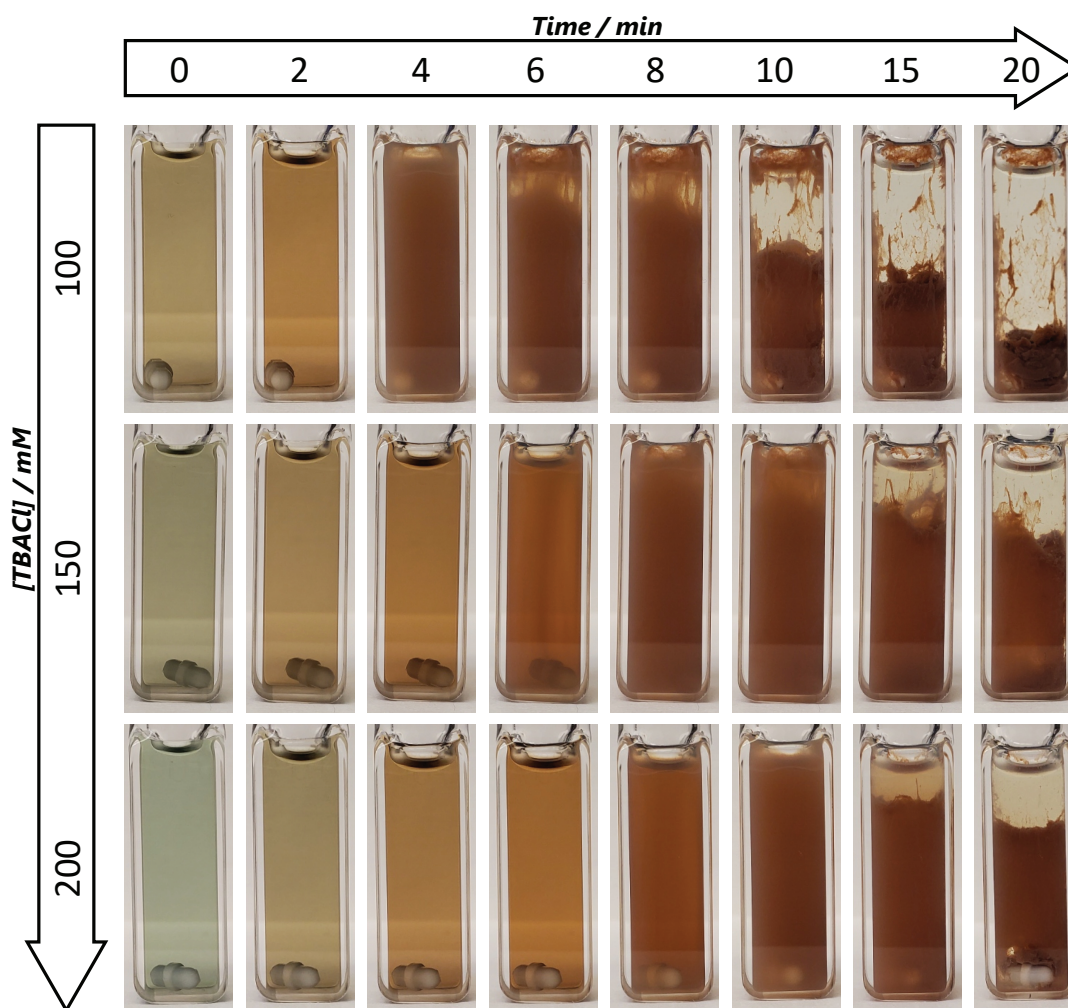
Fig. S19. Temporal changes of free-flowing nanocrystal dispersions initially at 90 °C as they are cooled at room temperature. Note that the sample with higher [TBACl] takes longer to gel due to their lower gelation temperature.
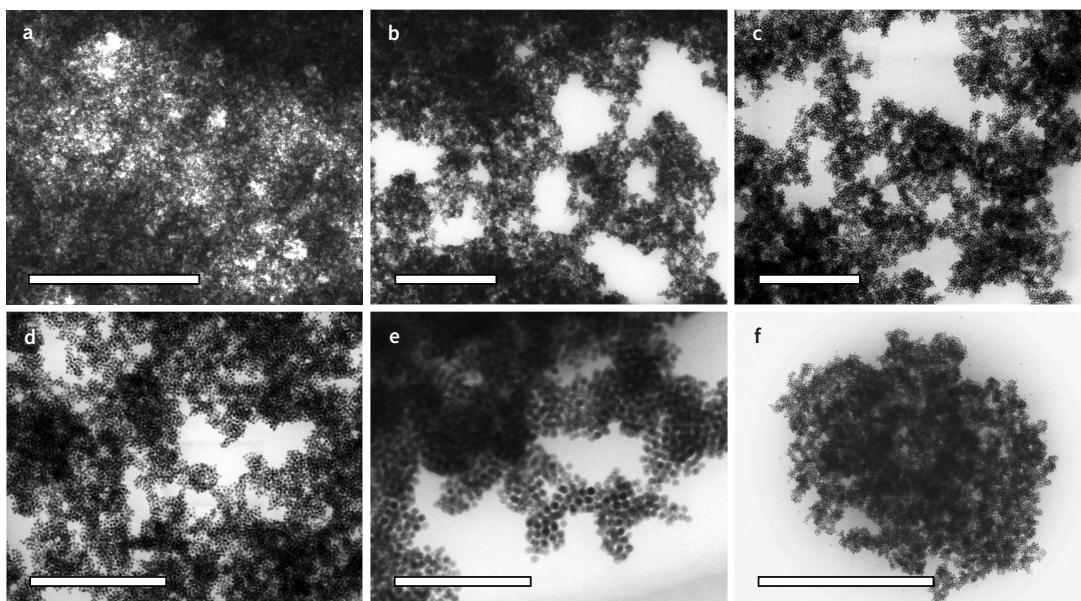
Fig. S20. STEM images of a TL-ITO gel. Scale bars are (a) 5 μm, (b) 1 μm, (c) 500 nm, (d) 500 nm, (e) 200 nm and (f) 1 μm
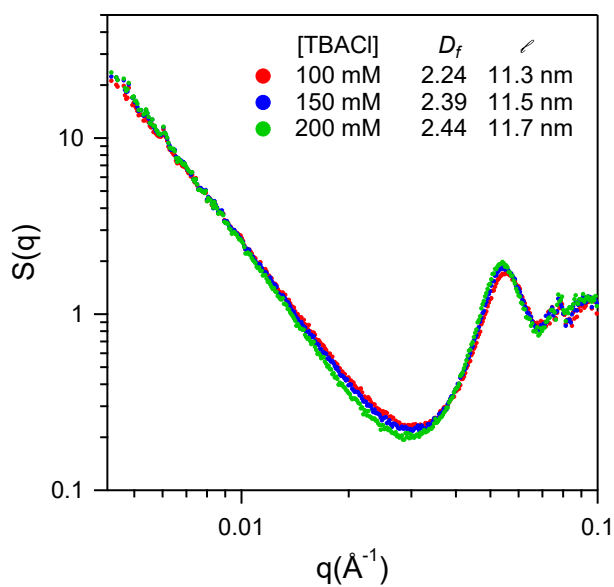
**Fig. S21. SAXS structure factor of TL-ITO gels with [TBACl] = 100, 150, and 200 mM.** Fractal dimension (D_f) and characteristic length (l) corresponding to the first peak were obtained from each structure factor.
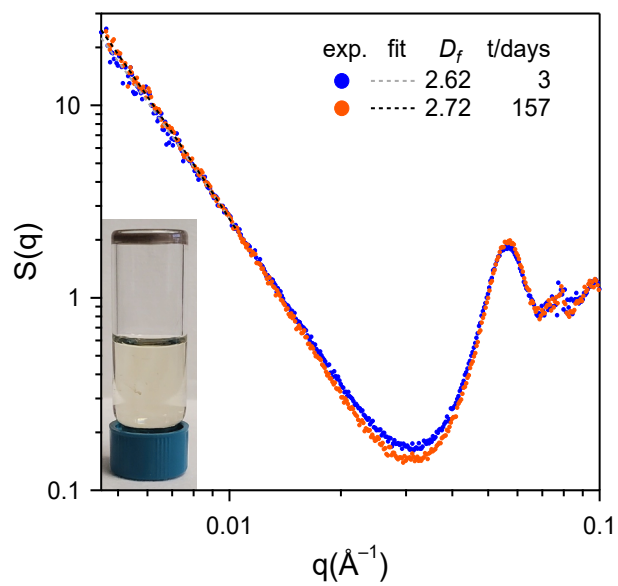
Fig. S22. SAXS structure factor of the [TBACl] = 150 mM sample 3 and 157 days after gelation. Inset photo shows the gel 157 days after gelation.
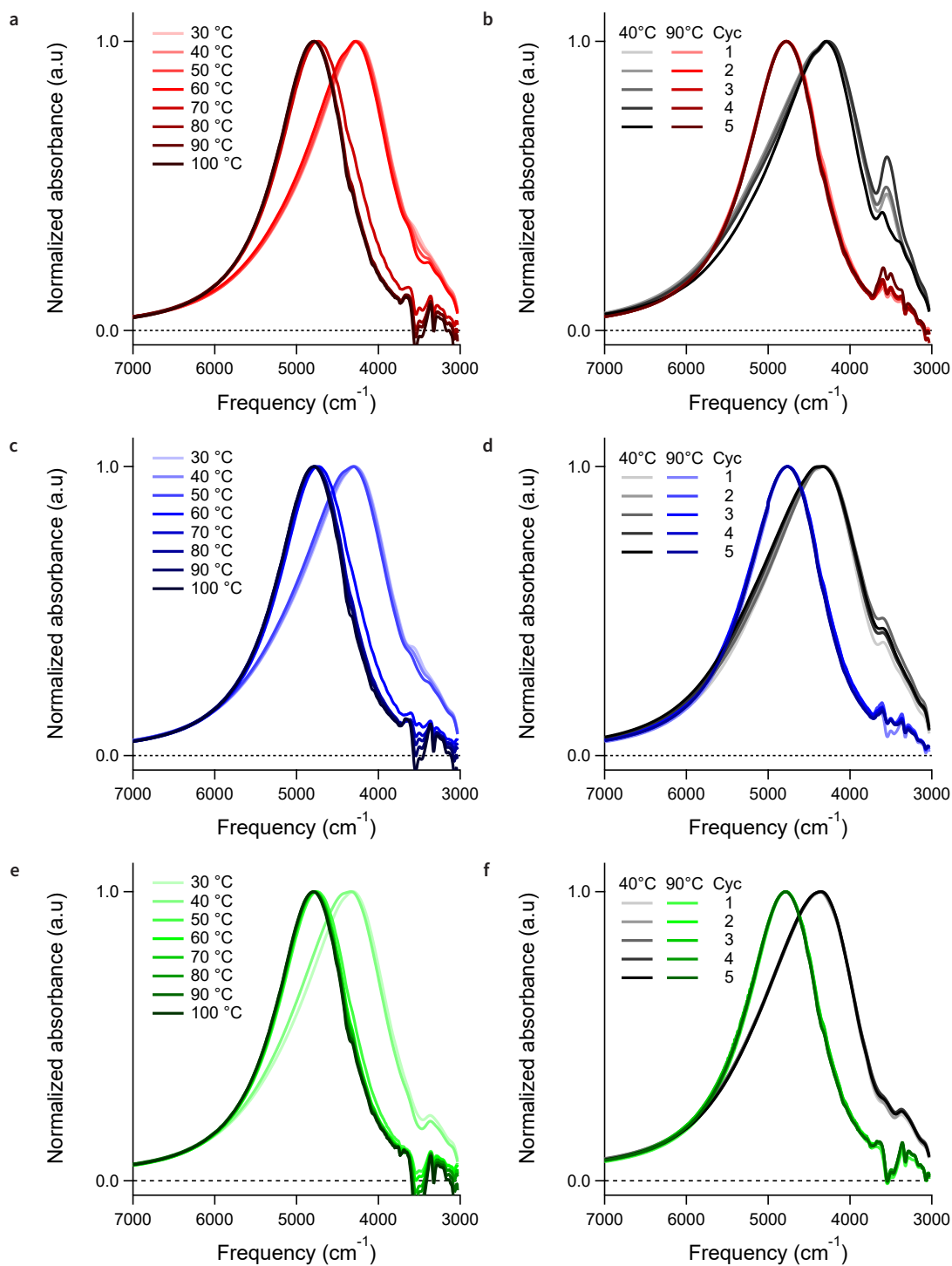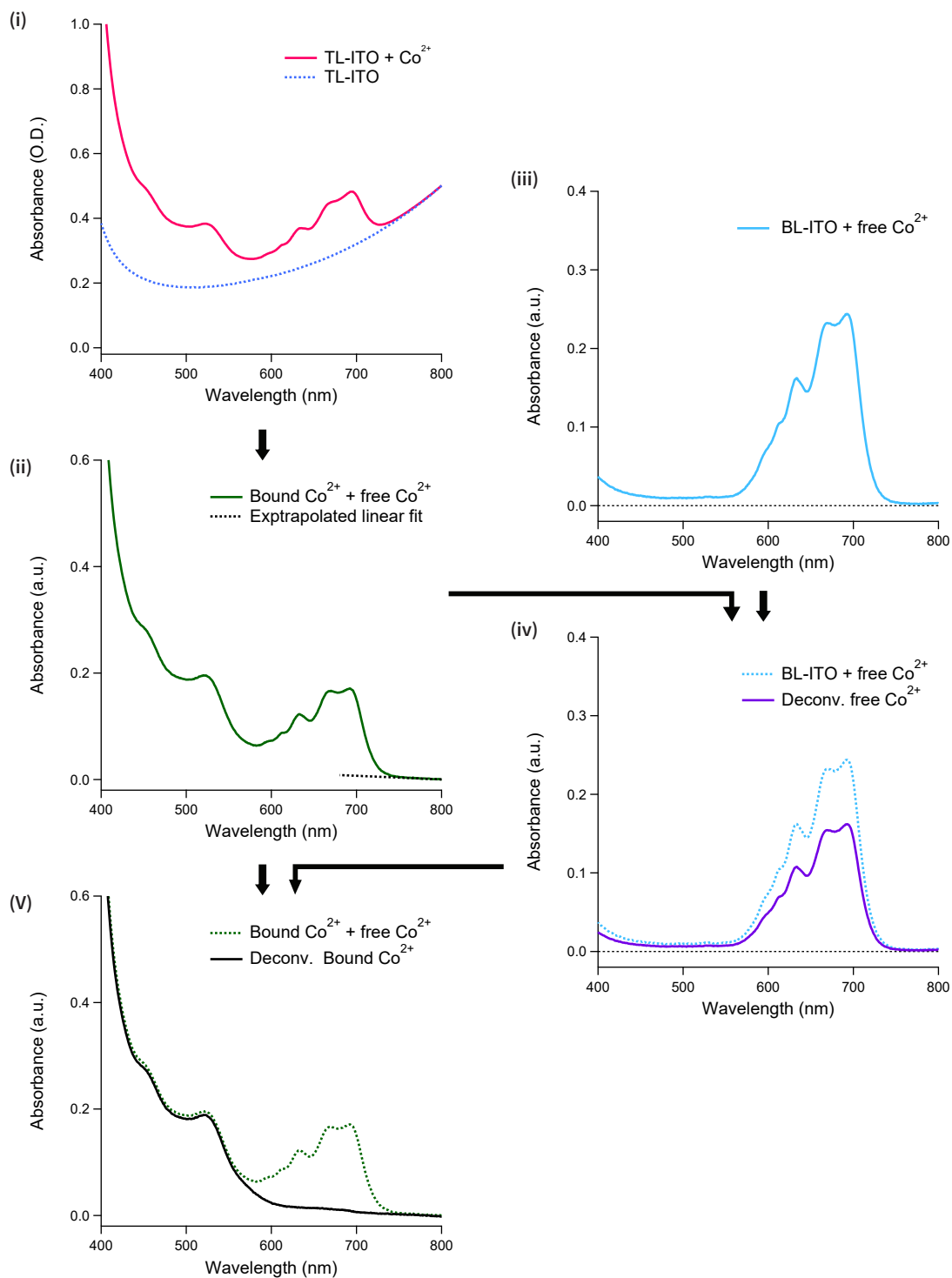
Fig. S23. Optical monitoring of thermoreversible nanocrystal assembly. LSPR absorption spectra at varying temperatures with [TBACl] = (a) 100, (c) 150, and (e) 200 mM measured *in situ*. LSPR absorption spectra during 5 cycles of heating to 90 °C and cooling to 40 °C with [TBACl] = (b) 100, (d) 150, and (f) 200 mM.
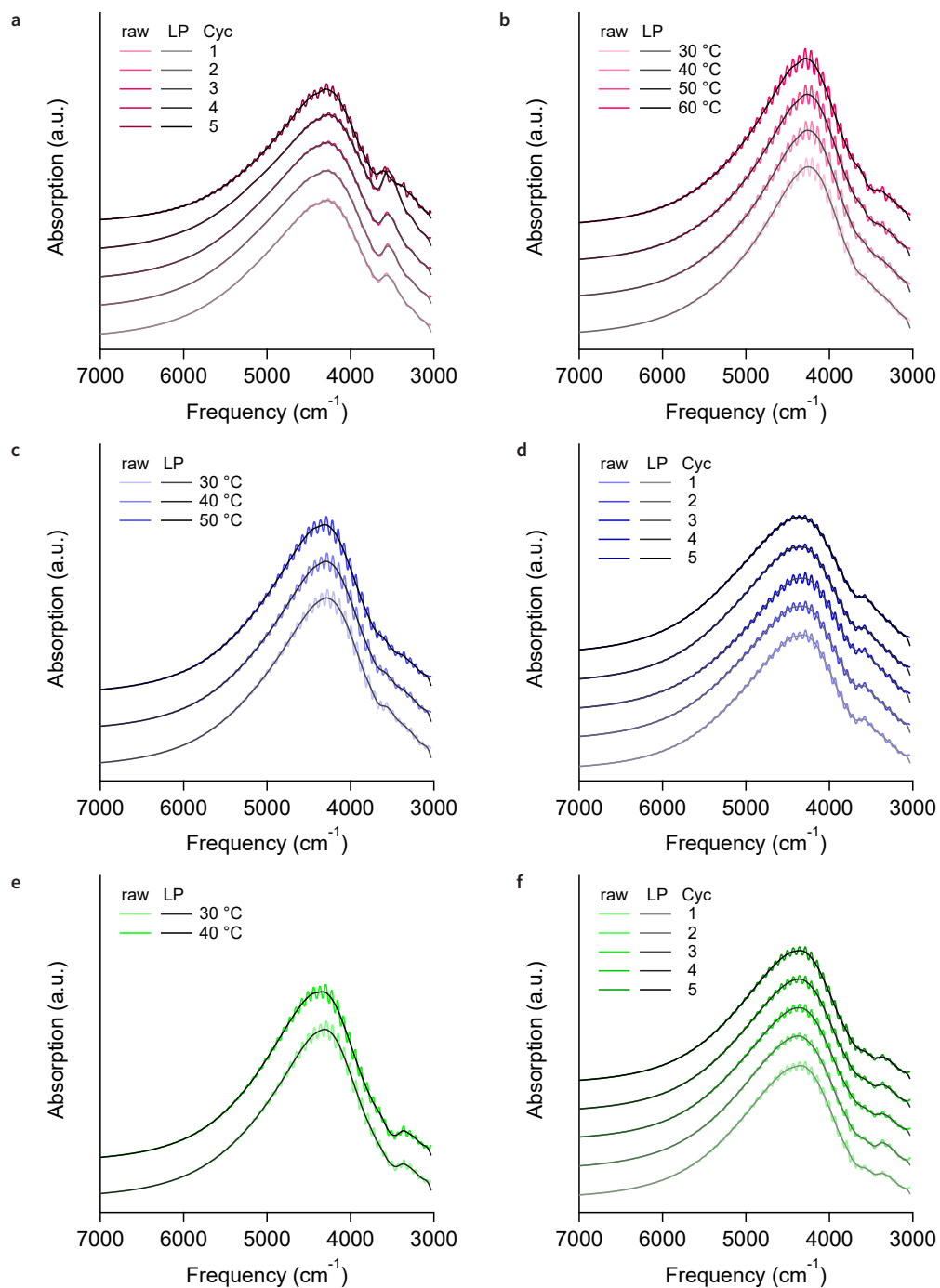
Fig. S24. Removing interference fringes from LSPR spectra of gels. A low-pass digital filter within *Igor Pro 8* was used to remove the interference fringes. *in situ* LSPR absorption spectra of gels with [TBACl] = (a) 100, (c) 150, and (e) 200 mM before and after applying the low-pass digital filter. LSPR absorption spectra of gels during 5 cycles of heating and cooling with [TBACl] = (b) 100, (d) 150, and (f) 200 mM before and after applying the low-pass digital filter.
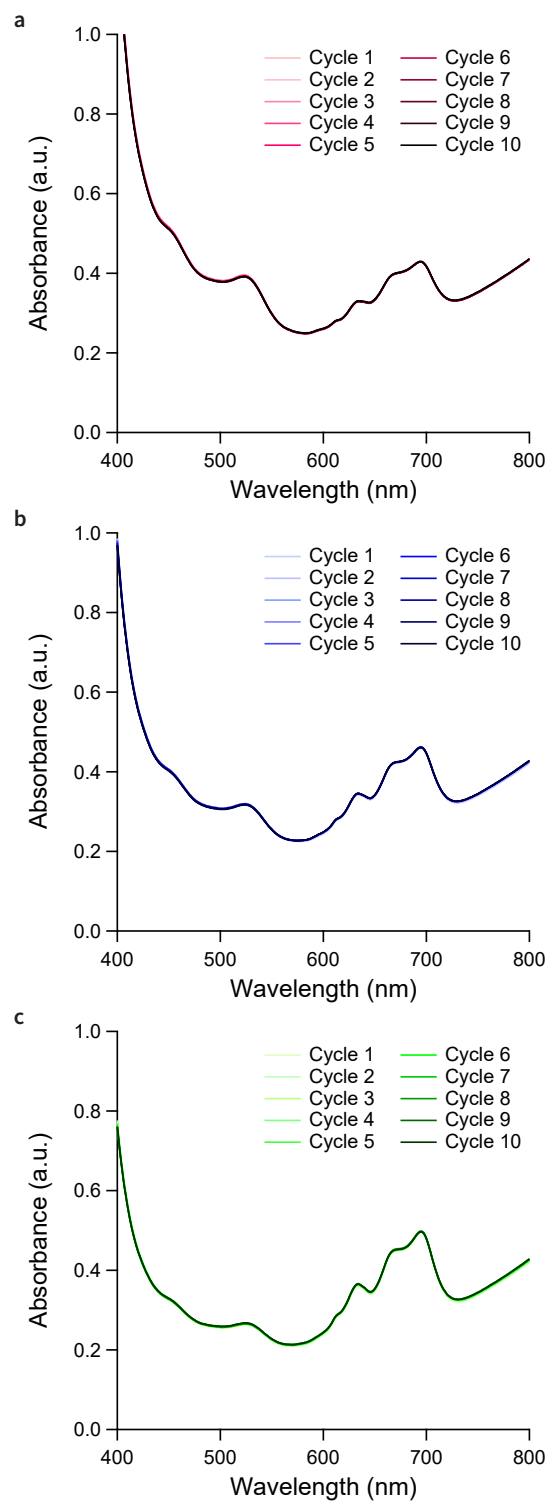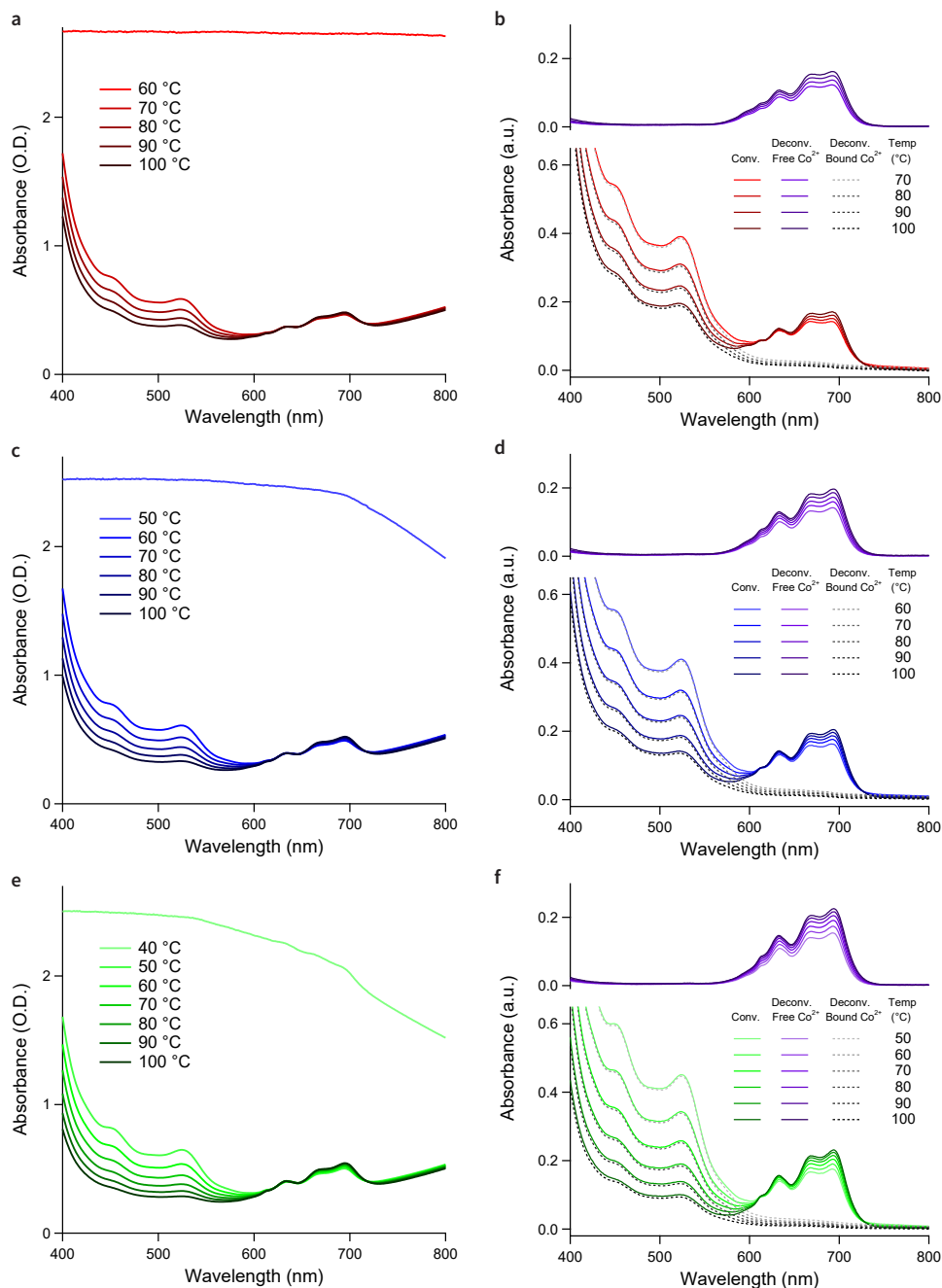
Fig. S25. Thermoreversibility of nanocrystal assembly. Visible absorption spectra of free-flowing nanocrystal dispersions at 90 °C with [TBACl] = (a) 100, (b) 150, and (c) 200 mM during 10 cycles of heating to 90 °C and cooling to 40 °C.
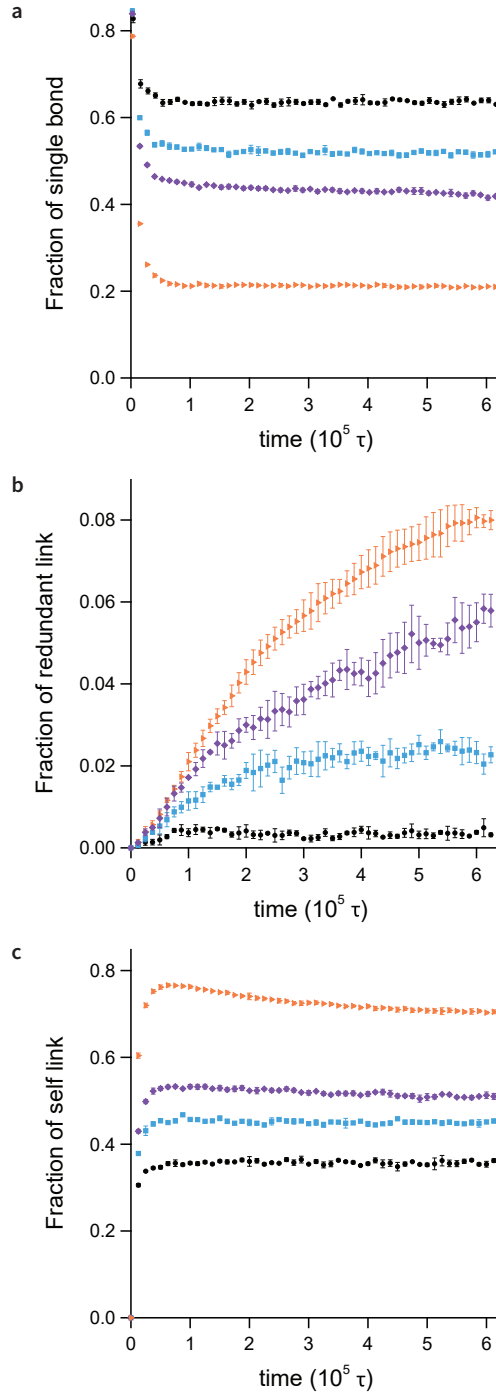
Fig. S26. Deconvolution of *in situ* visible absorption spectra of thermoreversible nanocrystal assembly. Detailed description can be found in Supplementary Text for *Deconvolution of in situ Visible Absorption Spectra*.

Fig. S27. Deconvolution of *in situ* visible absorption spectra of thermoreversible nanocrystal assembly. Visible absorption of nanocrystal assembly at varying temperatures with [TBACl] = (a) 100, (c) 150, and (e) 200 mM. Note that absorption spectra deviate significantly after gelation due to light scattering. Background-subtracted absorption spectra (bottom, solid) with deconvoluted absorption spectra of free Co^{2+} (top) and bound Co^{2+} (bottom, dash) of nanocrystal assembly at varying temperatures with [TBACl] = (b) 100, (d) 150, and (f) 200 mM.

Fig. S28. Schematic of nanocrystal-linker model used in MD simulations. Detailed description can be found in Supplementary Text for *Molecular Dynamics Simulations*.

Fig. S29. Fraction of different types of bonding motifs over simulation time. Bound linkers that form (a) single bonds, (b) redundant links, and (c) self-links. Temperatures $T/T_{gel} = 1.16$, 1.10, 1.05, and 0.89 are represented as black circles, blue squares, purple diamonds, and orange triangles, respectively. We set $T_{gel} = 0.093\varepsilon_b/k_{\mathrm{B}}$, which ensures that the fraction of bound linker matches the experimental value of 53% at the gelation temperature.
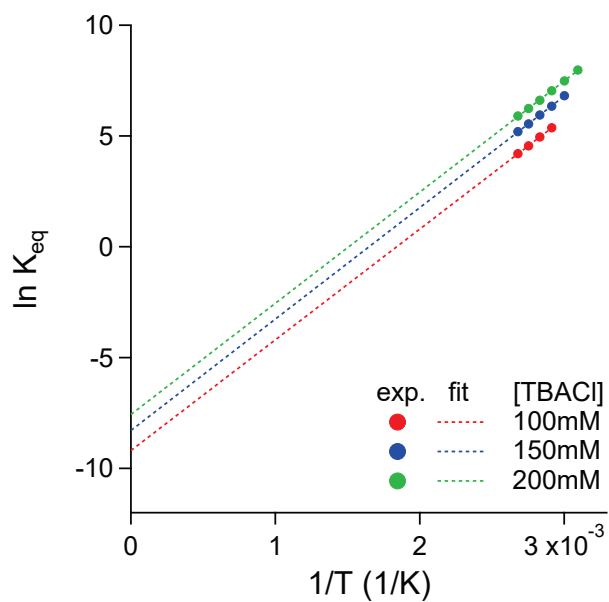
Fig. S30. van 't Hoff analysis of the equilibrium constant K_{eq} based on concentrations extracted from the spectroscopic deconvolution. The linear fits were extrapolated to obtain y-intercepts.
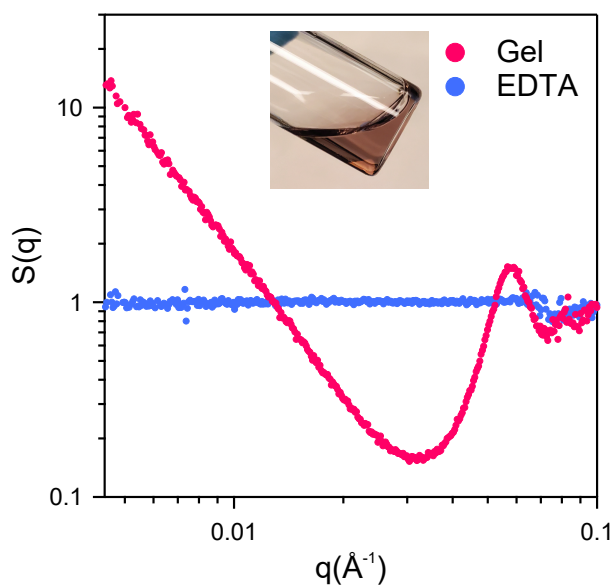
Fig. S31. SAXS structure factor of a TL-ITO gel before and after addition of EDTA. Inset photo shows a nanocrystal dispersion after the addition of EDTA.

Table S1: Thermodynamic parameters determined by van 't Hoff analysis. Gibbs free energy of reaction was calculated for a temperature of 50 °C.

[TBACl] / mM	slope	y-intercept	ΔH° / kJ mol^{-1}	ΔS° / J mol^{-1} K^{-1}	ΔG(50 °C) / kJ mol^{-1}
100	4997.2	-9.1966	-41.55	-76.46	-16.84
150	5027.9	-8.2907	-41.80	-68.93	-19.53
200	5016.9	-7.5687	-41.71	-62.93	-21.38
Average	5514.0	-8.3520	-41.7	-69.4	-19.25
Std. Dev.	12.7	0.6660	0.1	5.5	1.86

Table S2: The gelation temperatures (T_{gel}) determined from the sigmoid fits of LSPR peak positions (Fig. 3B). Note that the reported gelation temperatures are only approximate due to the large temperature increment (10 °C) between data points.

[TBACl] / mM	100	150	200
T_{gel} / °C	66	56	45

5. Supplementary Videos

Simulations start with purely repulsive interactions and attractions between patches are turned on to final values at time $t = 0$.

Video S1. a 100-nanocrystal simulation at temperature $T/T_{gel} = 1.18$ (dispersion).

Video S2. a 100-nanocrystal simulation at temperature $T/T_{gel} = 0.86$ (gel).